Double layer capacitance of a platinum electrode in a protic ionic liquid:

The influence of cation acidity

Klaus Wippermann, ** Yanpeng Suo, **, Christian Rodenbücher, ** Carsten Korte, ** and Alexei A. Kornyshev Christian Rodenbücher, ** Carsten Korte, ** and Alexei A. Kornyshev Christian Rodenbücher, ** Carsten Korte, ** and Alexei A. Kornyshev Christian Rodenbücher, ** Carsten Korte, ** and Alexei A. Kornyshev Christian Rodenbücher, ** Carsten Korte, ** and Alexei A. Kornyshev Christian Rodenbücher, ** Carsten Korte, ** and Alexei A. Kornyshev Christian Rodenbücher, ** Carsten Korte, ** and Alexei A. Kornyshev Christian Rodenbücher, ** Carsten Korte, ** and Alexei A. Kornyshev Christian Rodenbücher, ** Carsten Korte, ** and Alexei A. Kornyshev Christian Rodenbücher, ** Carsten Korte, ** and Alexei A. Kornyshev Christian Rodenbücher, ** Carsten Korte, ** and Alexei A. Kornyshev Christian Rodenbücher, ** Carsten Korte, ** and Alexei A. Kornyshev Christian Rodenbücher, ** Carsten Korte, ** and *

^a Forschungszentrum Jülich GmbH, Institute of Energy and Climate Research – Electrochemical Process

Engineering (IEK-14), 52425 Jülich, Germany.

^b Institute of Physical Chemistry, RWTH Aachen University, 52074 Aachen, Germany.

^c Department of Chemistry, Molecular Sciences Research Hub, Imperial College London, London, UK.

*Corresponding author; tel.: +49 2461 61 2572; fax: +49 2461 61 6695; email address:

k.wippermann@fz-juelich.de

Abstract

Protic ionic liquids (PILs) are promising candidates as electrolytes for future intermediate-temperature

polymer electrolyte membrane fuel cells (PEMFCs). A deeper understanding of their double layer

properties is essential for the improvement of oxygen reduction reaction (ORR) kinetics in the interface of

the platinum catalyst and PIL. In this study, we investigate the double layer differential capacitance of

platinum in the presence of PILs with acidic cations of various proton donor strengths as a function of the

electrode potential, bulk water content, and temperature. Complex capacitance plots of impedance spectra

enable the evaluation of a high-frequency double layer capacitance, C_1 , and a mid-frequency pseudo-double

layer capacitance, C_2 . The C_1 -capacitance curves were simulated by two mean field models that account

for the presence of water, short range correlations of ions, and, in the case of the second model, also for the

non-monotonic charging of the Pt surface that has a strong impact on the double-layer structure and

properties. The simulations reveal different double-layer properties of [2-Sema][TfO], a PIL with a highly

acidic cation, compared to the less acidic [1-EIm][TfO] and [Dema][TfO]. These variations are associated with differences in interionic forces, degrees of ion pairing, and the compactness of ionic layers. Most likely, these effects correlate with hygroscopicity and ability to form the hydrogen bonds of the cation, rather than with its acidity. The different pseudo-double layer capacitances of [2-Sema][TfO] and of the less acidic PILs at higher potentials are explained by different mechanisms of oxide formation.

Keywords: Double-layer capacitance; protic ionic liquids; cation acidity; potential of zero charge; interionic forces.

Highlights

- Double layer capacitance of PIL strongly relies on short range correlations of ions
- Simulated capacitances provide useful information about interfacial/bulk properties
- Non-monotonic charging involving up to 3 potential of zero charges was considered
- Acidity of the cation has no direct effect on the double layer properties
- The PIL cation affects Pt oxide film properties and mechanisms of oxide formation

1. Introduction

Protic ionic liquids (PILs) are promising candidates for use as non-aqueous electrolytes for future intermediate-temperature (IT) polymer electrolyte membrane fuel cells (PEMFCs). The structural and physical properties of the PIL will affect the double layer and electrochemical processes in the Pt catalyst/PIL interface. As for the low-temperature PEMFC, the oxygen reduction reaction (ORR) is still the bottleneck in the overall fuel cell kinetics and an improvement of ORR kinetics is desirable. This implies a better understanding of the double layer, in which the ORR and the preceding proton and oxygen transport takes place. Numerous articles on the double layer properties of ionic liquids have been published, of which only a limited number deal with ionic liquids that contain water [1–8]. The applicability of ionic liquids in PEMFCs was already demonstrated by Watanabe et al. in 2003 [9, 10] and the uptake of product water by the ionic liquids is unavoidable. Hence, further detailed investigations of different water effects are desperately needed if we are serious about the usage of PILs as electrolytes in PEMFCs.

Indeed, water molecules affect the double layer at the PIL/electrode interface in many respects. This includes a weakening of the ion—metal interaction and a distortion of the inner double layer structure caused by the preferential adsorption of water molecules on the electrode surface [3, 6] and the formation of networks of hydrogen bonds [7]. The coverage of water molecules was found to increase with the difference in the actual potential and the potential of zero charge (PZC), *i.e.*, the charge on the electrode surface [1, 2, 4]. Moreover, the adsorption of water molecules enables the formation of Pt hydroxides and oxides [11], narrows the electrochemical window (HER/OER) and causes pseudo-capacitances due to the formation of adsorbed hydrogen and oxygen species.

A key parameter of the double layer properties is differential capacitance. The analysis of impedance spectra in the complex capacitance plane (CCP) by means of the empirical Cole—

Cole type equation proposed by the Roling group allows for a distinction to be made between fast and slow capacitive processes [12]. In particular, a differentiation of 'true' double layer capacitances and pseudo-capacitances is possible. As described in the literature, the Gouy–Chapman–Stern theory that relies on an approximation for diluted solutions does not apply for the double layer capacitance in ionic liquids [13]. In 2007, Kornyshev developed a mean-field lattice gas model [13] for the capacitance of the electrode/ionic liquid interface. This theory predicts either 'bell'- or 'camel'-shaped *C/U* curves, depending on the so-called 'compacity' factor γ that reflects both the compactness of ion layers [13] and the degree of ion pairing [14–16]. The predicted curve shapes were experimentally-verified [4, 17–19]. Note that Kornyshev's initial theory [13] did not account for the presence of bulk water and short-range ion–ion interactions. The latter result in a so-called 'overscreening' effect, which means a higher screening by the ions than expected in light of a given surface charge [20–22]. The overscreening effect is particularly important at low and moderate surface charges and leads to a dramatic change in the double layer structure with alternating anion- and cation-rich layers that have been verified experimentally by means of AFS and XRD [23–32].

Friedl et al. were the first to simulate potential-dependent capacitance curves via a mean field model that considers bulk water and so the presence of water molecules in the double layer [4]. However, their simulations required considerable 'stretching' of the potential scale in order to obtain a good match between experimental and simulated data. They suspected that the stretching effect could be due to the non-consideration of short-range ion—ion interactions. This weak point was addressed in the modified mean field model of Goodwin et al. [33]: By introducing a 'correlation factor' α that accounts for short-range interionic forces, not only a stretching of the potential scale but also a decrease in the simulated capacitance closer to the experimental values was achieved [33]. Moreover, the correlation factor includes the dimensionless interionic force, and more precisely the difference of the repulsion and attraction

forces between the ions, (a–b), which can be evaluated in addition to the compacity factor, γ [33]. A combination of the models presented in the studies of Friedl et al. [4] and Goodwin et al. [33] would allow simulations that consider both the presence of water and short-range ion—ion interactions. Note that further studies [6, 8] have highlighted further details of the distribution of water in the electrical double layer of ionic liquids, and possible measures to control the population of water molecules at the interface. However, simple schemes of the noted combination could suffice for the first, simplified treatment of experimental data. Such simplification may be particularly beneficial in view of another important factor that will affect double layer capacitance, namely the charging behavior of the metal (here: Pt) surface, which adds to the complexity of the problem. Indeed, the common assumption is that the charge on the *bare* metal surface increases monotonically and more or less linearly with increasing negative or positive differences in the actual potential and the PZC.

However, if metal oxidation or even oxide film formation come into play, the picture changes: the charge on the oxidized surface turns from positive to negative and the charging behavior deviates from the simple, monotonic increase of charge with increasing potential with not one, but two different electrode potentials delivering zero charge of the electrode ("two PZCs") of the 'same' electrode, but eventually becoming different in the process of its charging. The non-monotonic charging of Pt and other Pt group metals was reported by Frumkin and Petrii back in 1975 [34]. Their radio tracer experiments confirmed Frumkin's earlier results, where he found two PZFCs (potential of zero free charge) corresponding to reduced and oxidized states of Pt [35]. Huang et al. validated Frumkin's results by modeling the metal/electrolyte interface considering surface oxides and the orientation of water molecules [36]. Note that they developed their model for diluted aqueous solutions, rather than for ionic liquids with limited amounts of water. Because Pt oxide is formed in the presence of water-containing ionic liquids as well, with possible electrosorption of water right onto the electrode

surface [6], one cannot exclude the non-monotonic charging of the Pt oxide surface in contact with the ionic liquid. Therefore, it seems to be reasonable to consider non-monotonic charging as well (see model2, below).

The focus of this work is the analysis of the differential double layer capacitance of the Pt/PIL interface using three PILs whose cations have different proton donor strengths, namely [Dema][TfO] (Diethylmethylammonium triflate), [1-EIm][TfO] (1-Ethylimidazolium triflate), and [2-SEMA][TfO] [37] (2-Sulfoethylmethylammonium triflate). The structure and pK_a values of the cations are shown in Fig. 1. More detailed information regarding the bulk and electrochemical properties can be found in a recent publication, in which the significantly different cation acidities of these PILs were proven to have a strong influence on the ORR rate [38]. Note that the cations differ not only in acidity but also in hygroscopicity [38, 39], the ability to form hydrogen bonds [38, 39], and in their interaction with the Pt surface (see below). The question is discussed as to whether and how these characteristics might correlate with the double layer structure and properties.

The potential-dependent high-frequency capacitance is simulated by two modified mean field models based on either monotonic (model1) or non-monotonic charging (model2) of the Pt electrode, which account for the presence of water in the double layer [4] and short-range ion-ion interaction [33]. To the best of our knowledge, this combined approach has never been used before. Also, for the first time, a non-monotonic charging of an electrode surface [36] was adopted for metal/ionic liquid interfaces (model2). Because the charging behavior determines the sign and amount of the surface charge, it will significantly affect local potential across the double layer, the dominating ion species in the innermost layer, the coverage and orientation of water molecules, and finally the entire structure of the double layer. The effect of the cation structure of the PIL, of the water content and temperature on the PZC, the compacity factor γ , the correlation factor α , and the dimensionless interionic force (a-b) is discussed. Finally, we

discuss the mid frequency pseudo-double layer capacitance, C_2 . In particular, the correlation of the C_2 –U curves with the cyclic voltammograms is studied and, depending on the type of cation, different mechanisms of Pt oxide formation are considered.

2. Experimental

PILs with the addition of water:

Diethylmethylammonium triflate ([Dema][TfO]) and 1-Ethylimidazolium triflate ([1-EIm][TfO]) with nominal purities > 98 wt% were used as received (IoLiTec-Ionic Liquids Technologies GmbH, Heilbronn, Germany). 2-Sulfoethylmethylammonium triflate ([2-SEMA][TfO]) was prepared in-house from triflic acid and N-methyltaurine by means of the method described in our previous publication [5]. These PILs, in particular [2-SEMA][TfO], are strongly hygroscopic. Utilizing Karl–Fischer titration, initial water contents of 0.25 wt% (3.2 mol%) for [Dema][TfO], 0.18 wt% (2.3 mol%) for [1-EIm][TfO], and 0.71 wt% (10.3 mol%) for [2-Sema][TfO] were determined. The PILs were mixed with Milli-Q[®] water to obtain 5–6 mixtures for each PIL in the range of the initial water content up to ≈50 mol% of water.

Measuring device:

Electrochemical experiments were performed with a Zennium electrochemical workstation (Zahner Elektrik GmbH, Kronach, Germany). A heating unit described in our previous publications [38, 40] was used to adjust the temperature in a range of 30–90 °C for [Dema][TfO] and [1-EIm][TfO], but 60–90 °C in the case of [2-SEMA][TfO]. This is because [2-SEMA][TfO] solidifies at temperatures below 60 °C, in particular at low water contents. In order to exclude atmospheric oxygen, purging of the compartment above the PIL/water mixtures with 10 ml/min dry nitrogen (99.999%) was commenced one hour before each

experiment. All measurements were performed in a 10 ml Pt crucible that served as both the electrolyte vessel and counter electrode [40]. The working electrode was a 1 mm Pt wire (99.95%, Goodfellow GmbH) with a length of 6.5 mm. The effective Pt electrode surface is 0.26 cm², taking into account a roughness factor of 1.29, was determined via hydrogen desorption. The reference electrode, a palladium—hydrogen electrode made of a 1 mm Pd wire (99.95%, Goodfellow GmbH), was self-prepared. Note that the Pd−H potential was ≈50 mV vs. RHE in diluted aqueous solutions, but less than 20 mV vs. RHE in PILs [40].

Methods:

Cyclic voltammetry

For each PIL, water content and temperature, CVs corrected by the iR drop with a sequence of 30 cycles were recorded with a scan rate of 0.1 V/s in a potential range of 0–1.6 V vs. Pd–H. The ohmic resistance was determined by means of impedance spectroscopy. The last, stationary cycle was analyzed and is discussed.

Electrochemical impedance spectroscopy (EIS):

Under the same conditions as described above, a series of 41 impedance spectra were recorded after each CV by gradually increasing the potential from 0 to 1.6 V vs. Pd–H with potential steps of 40 mV. A delay time of 30 s before each step assured stationary conditions. A frequency range of 1 Hz–100 kHz was chosen with an AC signal voltage amplitude of ± 20 mV. Altogether, it took about 70 minutes to record one series of EI spectra. The impedances were fitted as complex capacitances using the WinFit 3.5 software (Novocontrol Technologies, Montabaur, Germany). The three terms entered into the program (see Table S1, Supplementary data) rely on the empirical Cole–Cole-type equation noted above. However, valid capacitances could only be obtained for terms 1 and 2 (see the next chapter).

3. Results and discussion

Initially, representative impedance spectra of the three PILs are shown as complex capacitance plane (CCP) plots. Special emphasis was placed on the high- and mid-frequency capacitances, C_1 and C_2 .

3.1 The complex capacitance plots of impedance spectra

The impedance spectra recorded in a potential range of 0–1.6 V were displayed in the complex capacitance plane and analyzed using the empirical Cole–Cole-type equation proposed by the Roling group (see, *e.g.*, Drüschler et al. [12]). Fig. 1a–d shows typical CCP plots for a water content of ≈ 20 mol%, a temperature of 70 °C, and three selected potentials, each representing a specific potential regime (H_{UPD}, double layer charging, Pt oxidation; see the CVs in the inset pictures and Fig. S1 and Fig. S2 in the Supplementary Data). Note that the 'double layer charging' regime in the CVs (highlighted in red) refers to the anodic scan. Additionally, the molecular structures and pK_a values of the cations are shown.

In general, three capacitances can be distinguished that range from high (C_1) and mid (C_2) , to low frequencies (C_3) . The typical time constants of the associated capacitive processes are 0.1–1 ms (τ_1) , 1–10 ms (τ_2) , and 100 s (τ_3) . Fig. 1b shows the three capacitances for the example of [Dema][TfO] and U = 0.2 V. As only a small part of the l.f. (low frequency) semi-arc lies within the frequency window and it is difficult to attain accurate fit values, only C_1 and C_2 are discussed here. An interpretation of C_{1-3} was presented in our previous publication [5]: Whereas C_1 represents 'true' double layer behavior, i.e., ion movement and reorganization in the double layer, C_2 and C_3 are pseudo-double layer capacitances associated with the adsorption of charged species involved in Faradaic processes such as H_{UPD} , the formation of PtO_x , and the oxygen evolution reaction (OER).

The frequencies marked by the arrows indicate the transition between the high-frequency (h.f.) and mid-frequency (m.f.) semi-arcs ([Dema][TfO]) and ([1-EIm][TfO]) and the m.f. and low-frequency (l.f.) semi-arcs ([2-Sema][TfO]), respectively. In the latter case, the associated time constants of C_1 and C_2 differ by less than one order of magnitude. Depending on the PIL and the operation conditions, the m.f. semi-arc is not always obvious (such as in Fig. 1b). However, because the lower frequency limit was extended to 1 Hz (10 Hz in our previous publication [5]), valid C_1 and C_2 values could be obtained across the entire potential range measured.

The next chapter presents the main part of this work, namely the simulation of the high-frequency capacitance obtained from the CCP plots by means of the two modified mean field models mentioned above: Model1 is a combination of the modified mean field models proposed by Friedl et al. [4] (including the presence of bulk water) and Goodwin et al. [33] (considering short-range correlations, *i.e.*, interactions between the ions).

3.2 High-frequency capacitance, C_1

Essentially, the equations given in the Supplement of Friedl et al. [4] were modified by including the 'correlation factor' α introduced by Goodwin et al. [33] (see Eq. S1–7 in the Supplementary Data). Note that even taking into account short-range interactions between the ions [13] via the "renormalizing" α -factor, the resulting capacitances still come out somewhat higher than the measured ones. This may be cured by normalizing the simulated values of the potential-dependent capacitances via the experimental capacitance obtained at the U_{PZC} (see Eq. S1). Model2 is similar to Model1, but takes into account the occurrence of one or even two additional PCZ(s) that arise because of Pt oxide formation [36]. For both models, the following equation for the double layer differential capacitance adapted from the works of Goodwin et al. [33] and Friedl et al. [4] was used:

$$C(u) = \tilde{C}_w(u) \times \frac{\cosh\left(\frac{\alpha u}{2}\right)}{1 + 2\gamma \left[\sinh\frac{\alpha u}{2}\right]^2} \times \sqrt{\frac{2\gamma \left[\sinh\frac{\alpha u}{2}\right]^2}{\ln\left\{1 + 2\gamma \left[\sinh\frac{\alpha u}{2}\right]^2\right\}}}$$
(1)

Here, C(u) is the simulated capacitance, $\tilde{C}_w(u)$ is a pre-factor of the differential capacitance and α and γ are dimensionless parameters that take into account short-range correlations of the ions and the compactness of the ion layers, respectively. The pre-factor $\tilde{C}_w(u)$ includes dielectric properties and maximum ion concentrations of/in the double layer and their dependency on the water content (see Eq. S3–7 in the Supplementary Data). The key parameters included in Eq. 1 are the potential of zero charge, U_{PZC} , the correlation factor, α , and the compacity value, γ . These parameters are analyzed and discussed in detail in section 3.2.1. We will present a special discussion of α and γ —of the physics of these parameters as understood today, and of their values that provide best fits to the data. The potential of zero charge is not obvious from Eq. 1 but is included in u, the dimensionless potential drop in the double layer, according to $u \equiv (U-U_{PZC})/U_T$ ($U_T = k_BT/e \equiv$ thermal voltage). With this equation, the capacitance as a function of the electrode potential U is obtained. As noted above, normalization of the simulated capacitance is necessary. This is done by multiplying C(u) with the ratio of the experimental and simulated capacitance at PZC and yields normalized, simulated capacitances denoted as C_1 (see Eq. S1). More information about the parameters of Eq. 1 can be found in the Supplementary Data and the works of Goodwin et al. [33] and Friedl et al. [4]. In the following section, the simulations of the C_1/U curves based on Model1 are presented and discussed.

3.2.1 Model1: Modified mean field model, monotonic surface charging (one $U_{\rm PZC}$)

Model parameters

A proper combination of the values of U_{PZC} , α and γ is essential for achieving a satisfactory simulation, as these key parameters significantly influence the peak position and height of the

peaks or humps that occur in the double layer region of the C_1/U curves (see below). Whereas these parameters are free, other parameters included in the pre-factor $\tilde{C}_w(u)$ that are related to dielectric properties, ion geometries or water content, are fixed and set as follows:

- The (unknown) dielectric constants ε of the PILs were set to arbitrary values of 20 (less acidic PILs, [Dema][TfO] and [1-EIm][TfO]) and 40 ([2-Sema][TfO]); those of water were taken from literature [41]. The dielectric constant of 20 was chosen because for comparable PILs such as ethylammonium nitrate (EAN), a dielectric constant close to 20 was reported for temperatures higher than 40 °C [42, 43]. In the case of [2-Sema][TfO], a higher dielectric constant can be expected due to the polar sulfonic group in the cation. However, only ILs with OH-functionalized cations are reported to have ε values higher than 50 [44]. For this reason, an arbitrary value twice as high as that of the other PILs, i.e., $\varepsilon = 40$, was chosen. In order to check the sensitivity of the parameters α and γ on the chosen dielectric constant, simulations were carried out at various ε values. As can be seen in Fig. S3, α and γ change significantly at unrealistically—low ε values of < 20, but only a little at ε > 40. Moreover, satisfactory fits can only be obtained for $\varepsilon > 20$. The temperature coefficient of the ε of water is about -0.3 K^{-1} , whereas that of ILs is typically one order of magnitude lower or even positive [45]. For this reason and because the ε values and corresponding temperature coefficients of our PILs are unknown, we kept ε constant in the temperature range measured (ε of either 20 or 40).
- The volume ratio of a water molecule and the average volume of the PIL ions, ν , was calculated from the average v. d. Waals radii, resulting in values of 0.180 ([Dema][TfO]), 0.196 ([1-EIm][TfO]), and 0.173 ([2-Sema][TfO]).

- Following the approach of Friedl et al., $X_{\rm H2O}$, the ratio of the number of water molecules and the average number of ions in the double layer, was set to the bulk value under saturation conditions (high positive or negative charges) and to one tenth of the bulk value at the $U_{\rm PZC}$ [4]. A depletion of water at the potential of zero charge was validated by Feng et al. [1]
- In the case of [2-Sema][TfO], a higher water content in the double layer, particularly a higher coverage of water on the Pt electrode, in the presence of [2-Sema][TfO] compared to [Dema][TfO] [46], has been found. A probable reason for this is the special ability of [2-Sema][TfO] to form hydrogen-bonded networks [46]. This is accounted for by multiplying $X_{\rm H2O}$ with an arbitrary factor $f_{\rm x}=2$. The sensitivity of the parameters α and γ was checked for various $f_{\rm x}$ values (see Fig. S4). It turns out that factor $f_{\rm x}$ has only a moderate or even a small effect on α and γ . Good fits can be obtained across the entire range of $f_{\rm x}=0.1-3$.

These data, together with other structural data and electrochemical parameters derived from the analysis presented in the following, are summarized in Table 1.

Overview of the experimental and simulated C_1/U curves

The results are shown in Fig. 2 (variation of water content at the exemplary temperature of T = 90 °C) and Fig. 3 (variation of temperatures in the example of $x_{\rm H2O} \approx 20$ mol%). As was to be expected, a viable simulation of the experimental C_1/U -curves by means of Model1 is only possible in the potential range of the 'true' double layer behavior, *i.e.*, at potentials above the $H_{\rm UPD}$ region and below the onset potential of Pt oxidation.

In the H_{UPD} region, either a strong increase ([2-Sema][TfO]), a strong decrease ([Dema][TfO]), or a moderate decrease ([1-EIm][TfO]) of the h.f. capacitance is observed, with

the coincidence of the experimental and simulated data being poor. This is due to a dominating pseudo-capacitive process with an m.f. capacitance C_2 that is more than one order of magnitude higher than C_1 at the lowest potentials. Thus, the fit data of C_1 become partially erroneous, i.e., either they tend towards values typical for pseudo-capacitances or the h.f. semi-arc is masked by the m.f. one (C_2) . This results in either too high ([2-Sema][TfO], U = 0-0.2V) or too low ([Dema][TfO], U = 0-0.12V, [1-EIm][TfO], U = 0-0.04V) fit values of C_1 .

The increase of C_I at the onset of Pt oxidation (compare the CVs in Fig. 1) up to a maximum value and subsequent decrease is very similar to the approximately two-fold increase in double layer capacitance described by Breiter for $0.1-10 \text{ N H}_2\text{SO}_4$ [47]. Breiter explained this result by way of the reorientation of water molecules at the Pt surface and/or a substitution of large anions by small OH⁻ ions [47]. An alternative explanation is that a change in the sign of the surface charge induced by PtO_x formation [36] causes a reorientation of water molecules and a reorganization of the ion layers (including the diffuse part), and so a change in the compacity and the correlation factors (see below, Model2).

The influence of temperature, water content, and electrode potential on the double layer capacitance of ionic liquids is complex, as several factors with opposing effects must be considered. An increase in the temperature might cause:

- (i) A thinning of the double layer because of thermal dissociation of ion associates \rightarrow increase of C_1 [19];
- (ii) An increase in the water adsorption/incorporation \rightarrow thickening of the inner double layer [3] and an increase in the average permittivity \rightarrow increase or decrease of C_1 [5, 40]; and
- (iii) A decrease in γ [33], probably caused by increasing ion pairing [48] \rightarrow increase of C_1 .

(iv)If C_1 includes pseudo-capacitances in the H_{UPD} region: decrease in the H_{UPD} charge and the pseudo capacitance \rightarrow decrease of C_1 [5].

With respect to ion pairs, their simple interpretation as separate neutral units is doubtful, as each ion interacts with several others (and water, if present) and the simulated lifetime of ion pairs is very short, in the range of 10^{-12} – 10^{-10} s [49, 50]. An increasing bulk water content causes a similar effect as the one explained in point (ii), but is probably more pronounced. Conversely, for (iii) and (iv), the opposite effects on C_1 are expected. This is because by increasing the water content, ion pairing generally decreases [51] and the pseudo-capacitance in the H_{UPD} region increases [5]. Moreover, we have adopted the notion of a depletion of water around the PZC and increasing water adsorption/accumulation in the double layer with increasing positive or negative charge up to a saturation value [1, 4]. The dependence of the amount of water on the electrode potential, here denoted as X(u), is given by Eq. S6. Because X(u) is the only potential-dependent parameter in the equations that describe the potentialdependence of the dielectric constant, ε , and of the average ion concentration, \bar{c} (eqs. S4, S5), the dependencies $\varepsilon(u)$ and $\bar{c}(u)$ are substantially influenced by X(u). As can be seen in Fig. 2 and Fig. 3, the three PILs show significant differences in the h.f. capacitance as a function of U, T and $x_{\rm H2O}$. In the following, we highlight these differences in a discussion of the important fitting parameters U_{PZC} , α , and γ .

Potential of zero charge, $U_{\rm PZC}$

The PZCs of the PILs used for the simulations vary in the order $U_{PZC,[2-Sema][TfO]} = 0.28 \text{ V} < U_{PZC,[Dema][TfO]} = 0.36 \text{ V} < U_{PZC,[1-EIm][TfO]} = 0.44-0.48 \text{ V}$. Note that these values were not experimentally-determined but produced the best matches of the experimental and simulated data. The U_{PZC} depends on the PIL but seems to be virtually independent of the water content and temperature. One might expect a temperature-dependence of the PZC if the adsorption of

either the cations or [TfO]⁻ anions would be temperature-dependent. This is obviously not the case.

 $U_{\rm PZC}$ values of around 0.3 V / RHE [52–54] for Pt in aqueous acidic solutions and a potential of zero total charge (PZTC) value of 271 ± 9 mV / RHE for [Dema][TfO] [55] have been reported. Because of the small potential difference (≈ 0 –20 mV [40]) of the RHE and the Pd–H reference electrode in highly concentrated electrolytes, the $U_{\rm PZC}$ values for [Dema][TfO] and [2-Sema][TfO] used for our simulations are close to the reported value of about 0.3 V, indicating an almost symmetrical adsorption of the ions. Conversely, the significantly higher PZC of [1-EIm][TfO] suggests a stronger interaction of the [1-EIm] $^+$ cations with Pt compared to [TfO] $^-$ (asymmetric adsorption [56]) and the other cations. According to the literature, this may be due to a stronger interaction of the imidazolium ring with the Pt surface. For example, Every and Zawodzinski found a decrease in platinum activity when adding alkyl-substituted imidazoles to acid solutions [57]. They explained this effect by way of the adsorption of imidazole on the platinum surface and the interaction of the π electrons of the aromatic ring with Pt. Meanwhile, Eschenbacher et al. have shown that imidazolium ions adsorb more strongly on Pt(111) than non-aromatic pyrrolidinium ions, which do not have π electrons [58].

However, if [1-EIm]⁺ interacts more strongly with the Pt surface than [TfO]⁻, one would expect a dependence of U_{PZC} on the water content, *i.e.*, the highest PZC for neat and the lowest PZC for highly diluted [1-EIm][TfO]. This is clearly not the case here. In fact, only the PZC of [1-EIm][TfO] with ≈ 50 mol% water of 0.44 V is slightly smaller (40 mV) than that of the other water concentrations (2.5–42 mol%). One possible explanation of this—apparent—contradiction lies in the assumption that the water concentration in the innermost layer and on the Pt surface in the potential range around the U_{PZC} is much smaller than the bulk value. Thus, there is a severe damping effect of a changing bulk water/ion concentration in the double layer at potentials around the U_{PZC} . This hypothesis is confirmed by our simulations, where the ratio

of the concentration of water in the depletion region near the $U_{\rm PZC}$ and in the saturation region at high surface charges was set to 0.1 in order to obtain a good match of experimental and simulated data. A depletion of water around the $U_{\rm PZC}$ [1] was one of the approximations used by Friedl et al. [4] for their calculation of C/U curves. Apart from a change in the ion concentration, the contribution of water dipoles to the $U_{\rm PZC}$ is known to be small or even negligible for metals with relatively high effective electronegativities, such as Pt[59]. In summary, the different PZCs of the three PILs are probably not due to (small) differences in the (small) coverage of water molecules around $U_{\rm PZC}$.

A higher $U_{\rm PZC}$ means a less positive surface charge in the typical potential range of fuel cell cathode operation of about 0.8–1 V and so a higher concentration of cations near the Pt surface that may enhance the ORR current density via the presence of a larger number of (potential) proton donors. However, due to their low acidity, [1-EIm]⁺ ions are practically inactive as proton donors in the ORR [38]. On the contrary, [1-EIm]⁺ ions may block the Pt surface with respect to oxygen and water adsorption.

There is another reason why the coverage of water molecules should be smaller in the case of [1-EIm][TfO]: MD simulations revealed a stronger interaction of water molecules with the anions than the cations [60, 61]. Thus, we might expect an especially strong increase in the water concentration in the anion-rich layer that forms on the positively-charged Pt surface. In the case of [1-EIm][TfO], the higher PZC implies a lower positive surface charge at typical cathode potentials of 0.7–0.8V. This means a lower concentration of anions and, in accordance with the above hypothesis, a smaller amount of water molecules in the innermost layer. This assumption is supported by a higher onset potential of the Pt oxidation and a smaller PtO_x reduction charge for [1-EIm][TfO] compared to the other PILs (see CV plots in the inset pictures of Fig. 1). It should, however, be considered that the water content of the double layer is not only affected by the surface charge and the cation—Pt interaction. The hygroscopicity and

the ability to form hydrogen bonds is important as well. The latter effects support the assumption of a higher water content in the case of [2-Sema][TfO], which has five sites available for hydrogen bonding.

In summary, [1-EIm][TfO] stands apart from the other PILs due to its relatively high PZC, which is largely independent of the bulk water content. This result can be explained by the combination of a stronger interaction of the cation with Pt and a lower water content in the double layer. By contrast, the cation acidity does not play a decisive role. In addition to the Pt–ion interactions, ion–ion interactions will also have an impact on the double-layer properties. The short-range correlation of ions, represented by the correlation factor α , will be discussed in the next section.

Correlation factor, a

The correlation factor α , introduced in [33], accounts for the short-range correlation/interaction of ions, *i.e.*, Coulombic repulsion and attraction forces beyond their account in the mean-field approximation, as well as short-range steric repulsion beyond the excluded volume mean-field description. If, for the sake of simplicity, the dimensionless constants that represent the Coulombic repulsion forces between cations, a_+ , and between anions, a_- , are set equal, *i.e.*, $a = a_+ = a_-$, the following equation is obtained [33]:

$$\alpha = \frac{1}{1 + \frac{\gamma}{2}(a - b)} \tag{2}$$

Here, b is the dimensionless constant that is established by short-range attraction and steric repulsion forces between cations and anions. As pointed out by Goodwin et al. [33], repulsion forces dominate, *i.e.*, a > b. Thus, α must always be smaller than one. Short-range repulsion forces impede the screening of the surface charge and lead to a decrease in the potential drop across the double layer [33]. In our case, α factors in the range of 0.1–0.22 were obtained

because the potential drop was about 5–10 times smaller. As noted above, the modified mean field model presented by Goodwin et al. does not explicitly take into account the overscreening effect that results in alternating, anion- or cation-rich layers and thus oscillating potential profiles (see *e.g.*, Fedorov and Kornyshev [20]).

The dependence of the correlation factor on the temperature and water content is depicted in Fig. 4a/b. This may be a trivial consequence of the definition of a and b, the quantities already normalized to k_BT , i.e. $a \propto 1/k_BT$, $b \propto 1/k_BT$, and if $\frac{\gamma}{2}(a-b) \gg 1$, $\alpha \propto$ k_BT . The effect of temperature, as we see in this figure, is more pronounced than that of water: whereas α increases almost linearly with temperature, there is only a slight tendency of α to increase with the water content. In general, the correlation factors of [2-Sema][TfO] tend to be somewhat higher and the α -T and α - x_{H2O} profiles of [2-Sema][TfO], which appear different compared to those of the less acidic PILs. This becomes particularly apparent in the linear fits of the α -T profile of [2-Sema][TfO]: the slope and therefore the intercept at α =0 ($T(\alpha$ =0) = 262 K) is significantly higher than those of [Dema][TfO] ($T(\alpha=0) = 192$ K) and [1-EIm][TfO] $(T(\alpha=0)=211 \text{ K})$. The intercept temperature $T(\alpha=0)$ is an extrapolated, virtual value that would arise at infinitely high a-b values (see Eq. 2). Although the physical meaning of $T(\alpha=0)$ is unclear, it is interesting to note that the mean Vogel (or ideal glass transition) temperature T_0 derived from the VFT plots of the total conductivity of [2-Sema][TfO] at different water contents of up to \approx 50mol% is significantly higher as well ($T_0 = 202\pm4$ K compared to 144 \pm 16 K ([Dema][TfO]) and 143 ± 7 K ([1-EIm][TfO])[62]). A higher T_0 is usually associated with stronger interionic interactions [63].

Because α depends on the compacity factor γ and the difference of repulsion and attraction forces, a-b, plots of γ and a-b vs T and x_{H2O} will help unravel the nature of the effects of temperature and water content on these parameters (see Fig. 5). As is shown in [33],

the effect of α on the differential capacitance is strong around U_{PZC} and small at high(er) positive or negative electrode polarizations. For this reason, we chose γ and a-b values at PZC. As α is inversely proportional to γ and a-b, it made sense to plot the inverse values of γ and a-b as well (see Fig. 5b/d).

It is evident from Fig. 5a that the $(a-b)_{PZC}$ values decrease in the same order as the $T(\alpha=0)$ ones obtained from the α -T plots, *i.e.*, [2-Sema][TfO] > [1-EIm][TfO] > [Dema][TfO] (see also Table 1). This supports the assumption that the interionic forces might be higher in the case of [2-Sema][TfO] compared to [Dema][TfO] and [1-EIm][TfO]. However, because the α values of the three PILs are comparable, there must be a compensation effect. Indeed, the compacity values of [2-Sema][TfO] are the lowest and those of [Dema][TfO] the highest. With the exception of [Dema][TfO], the γ_{PZC} -T plots of the other PILs exhibit a decrease in γ_{PZC} with temperature. Because the degree of ion-pairing should decrease with temperature and thereby lead to increasing γ_{PZC} values, this result is somewhat unexpected (for a detailed discussion, see the section 'compacity value' below).

For [2-Sema][TfO], the inverse plots in Fig. 5b show a six-times-larger slope $d\gamma_{PZC}^{-1}/dT$ compared to [1-EIm][TfO] (that of [Dema][TfO] is even negative!), but a two times ([Dema][TfO]) or only 10% ([1-EIm][TfO]) smaller slope $d(a-b)_{PZC}^{-1}/dT$ compared to the other PILs. This results in a steeper slope $d\alpha/dT$ for [2-Sema][TfO]. A comparison of the $d\gamma_{PZC}^{-1}/dT$ and $d(a-b)_{PZC}^{-1}/dT$ slopes shows that the effect of temperature on the correlation factor α is dominated by the temperature-dependency of both γ and a-b in the case of [2-Sema][TfO] and that of a-b for the low acidic PILs.

In summary, [2-Sema][TfO] forms double layers with the highest interionic forces but the lowest compacity values, *i.e.*, two effects that compensate each other and lead to similar correlation factors for the three PILs. Although the size of the interionic forces and compacity

values follows the cation acidity, the latter does not play a (major) role. As will be shown in the next section, ion-pairing/clustering and the concentration of free ions rather than the compactness of the ion layers affects the compacity values of the PILs.

Compacity value, γ

Subject to [33] (see also Eq. S7 in the Supplementary Data), γ depends on the compacity values of the anions and cations, γ - and γ +, as well as the potential drop u and the correlation factor α . The fitted values γ - and γ + serving as functions of temperature and water content are shown in Fig. 6 and the resulting, overall γ values for the different electrode potentials can be seen in the γ /xH2O- and γ /T-plots in Fig. S5 and Fig. S6.

To better understand these results, we must look into the updated interpretation of compacity. In accordance with earlier studies [14–16], the meaning of γ is the ratio of the average concentration of *free* ions in the bulk to the maximum possible concentration of ions. As in the bulk, according to the estimates of [14], on average only 15–20% of ions are free and the rest of them are clustered in ion pairs or highly electroneutral large clusters, γ should lie in the range of 0.15–0.2. Moreover, the balance of ions being free or clustered shifts towards free ions with increasing temperature. In this relationship, the 'ionic semiconductor concept' was proposed [64] even earlier than those studies, but was rationalized and quantified in [14]. It rests on the idea of dynamic equilibrium between two ionic states: clustered state, equivalent to a valence band, and a free ion state, equivalent to a conduction band. The two states are separated by a narrow band gap on the order of $k_B T$. Thus, γ is expected to become higher with temperature. However, there could be competing and side effects, complicating the temperature effect on γ . Moreover, when charging the double layer, the clusters within it will become

cracked as the presence of monopoles in the double layer region is more favorable than dipoles, quadrupoles, or any other multipoles.

As noted above, the negative (cathodic) wing of the camel-shaped curves is masked or distorted by pseudo-capacitive processes such as H_{UPD} . Therefore, a precise evaluation of the γ_+ values is not possible. Rather, they serve to 'shape' the anodic wing of the simulated curves, particularly at low positive charges (at high positive charges, the effect of γ_+ is small). As is shown in Fig. 6, the γ_+ values are always higher than the γ_- ones. Qualitatively, this corresponds to the higher average radii and volumes of the larger cations [13]. A quantitative correlation is not possible due to the aforementioned inaccuracy. The small γ_- values of all of the PILs make sense if we view those values as the ratio of free anions to their maximal possible concentration in the double layer, but in some cases they seem to be too small. This is especially true for [2-Sema][TfO], where the lowest γ_- value is only 0.062. Naturally, together with low γ_+ values, this leads to the capacitance curves having a camel-shape across the entire potential range investigated. The same is true for [1-EIm][TfO], whereas the C/U curves of [Dema][TfO] show both bell- and camel-shaped behavior, depending on the temperature and water content (see figures 3a and 2b as well as Fig. S5 and Fig. S6).

It is clear that the compactness of an ion layer near the interface cannot possibly be one order of magnitude higher or even more than that in the bulk electrolyte. However, it is the ion pairing/clustering that produces a certain amount of 'neutral blocks' that can be expelled from the double layer and is responsible for smaller concentrations of 'free' ions. Because both γ - and γ + are proportional to the average concentration of free ions in the bulk, the compacity factors must decrease with an increasing extent of ion pairing/clustering at a given maximum ion concentration of such ions in the double layer (see Eq. S7). The ratio of the effective van der Waals volumes of the cations and [TfO] $^-$ is only 1.36 ([Dema][TfO]), 1.24 ([1-EIm][TfO]) and 1.57 ([2-Sema][TfO]). Therefore, it is considered unlikely that the maximum concentration

of the cations is much smaller than that of the anions, as would be expected for large cations and that would lead to a high ratio γ_+/γ_- . Indeed, 1.1–3 times higher γ_+ than γ_- values are obtained for the PILs. As noted above, a precise evaluation of γ_+ is not possible and so the 'true' γ_+ values might be higher or smaller. This explains deviations in the ratio γ_+/γ_- from those expected due to the ratio of the van der Waals volumes of the cations and [TfO]⁻, as well as too low or too high γ values compared to the expected range of 0.15–0.2.

Because the concentration of free ions should increase with increasing temperature and water content [48, 51], one would expect a similar dependence for γ_- , γ_+ and γ (see above). Inspection reveals that with the exception of the temperature-dependent γ - values of [Dema][TfO], this is not the case. Although the γ_+ values of all PILs are virtually independent of the temperature and water content, the γ - values of [2-Sema][TfO] and [1-EIm][TfO] tend to decrease with increasing temperature and water content, in contrast to what would be expected. Clearly, there exists an effect that compensates for the change in the concentration of free ions. An important factor here is the water content in the double layer. A former investigation of the oxygen reduction reaction on Pt in [2-Sea][TfO] provided indications that, at a given bulk water concentration, the water content in the double layer increases with increasing temperature [40]. The uptake of water into it would not only cause a decrease in the maximum possible concentration of ions, but—even more importantly—could also lead to structural changes due to hydrogen bonding, which in turn favors the formation of ion pairs/clusters (see below). This would explain the observed dependencies of the γ values in the range of temperature and water contents investigated here. Moreover, the especially pronounced decrease in γ and γ with increasing temperature in the case of [2-Sema][TfO] (see Fig. 5a/6a) supports the assumption that the water content in the double layer relative to the bulk electrolyte is highest for [2-Sema][TfO]. However, at even higher bulk water contents (>> 50mol%), the increase in free ions due to hydration should become the dominating effect and result in an increase in the

compacity factor. Note that the actual model neither accounts for a temperature dependency of the water content in the double layer nor the structural changes induced by the uptake of water. A quantitative determination of the content and distribution of water and a detailed study of the double layer structure is beyond the scope of this work and will form part of future investigations.

In any case, the lowest γ values are obtained with [2-Sema][TfO], suggesting a larger ion pairing/clustering effect compared to the other PILs. This is supported by the stronger influence of the fitted values of γ on the temperature dependence of the fitted values of the correlation factor α (see Fig. 4/5). A possible reason for this might be the particularly pronounced ability of [2-Sema][TfO] to form hydrogen bonds, as the quantum chemistry calculations of Zhang et al. [65] revealed that hydrogen bonding induces the formation of ion pairs. Keeping in mind that the fitted values of correlation factor α is similar for all three PILs, the stronger interionic forces in the case of [2-Sema][TfO] are obviously compensated by a higher degree of ion pairing/clustering. This is not self-explanatory, as a lesser amount of free ions would suggest weaker interionic repulsion forces.

It is clear that such interrelationships are complex, including several superimposed effects such as the short range interactions between the free ions (a - b !), structural changes like the reorientation of ions, or the formation of hydrogen bonding networks via water molecules together with ion pairing. These effects cannot be easily unraveled without further investigations.

Likewise, the role of cation acidity on double layer capacitance remains unclear, as other properties like cation structure, cation—Pt interaction or hygroscopicity and the ability to form hydrogen bonds are important as well. This differs from the influence of cation acidity on ORR, where a clear advantage of highly acidic cations regarding the ORR rate constant of the r.d.s. and the overall ORR kinetics has been demonstrated [38]. A highly acidic cation like [2-Sema]⁺

also favors a fast proton exchange between the cation and water, and so cooperative proton transport [66]. The effects listed in Table 1 could suggest that the cation acidity does not play a role. However, there are several parameters that either change in the order of cation acidity (highlighted in green) or show a distinctly different value for the acidic [2-Sema][TfO] (highlighted in blue). Because a high local charge density on the cation will increase both the Coloumb interaction and cation acidity, the latter should be indirectly linked to the effects specified in Table 1, namely interionic forces, compacity of the ion layers, and ion pairing.

In summary, [2-Sema][TfO], the PIL that contains a highly acidic cation based on methyltaurine displays stronger interionic forces, more compact ion layers, and a greater tendency of ion pair formation compared to the less acidic [1-EIm][TfO] and [Dema][TfO]. There is an indirect connection, but no causal link between these properties and the cation acidity. This differs from the direct correlation between the ORR rate and cation acidity reported previously [38]. Rather, it is likely that the direct causes are the hygroscopicity and hydrogen-bonding ability of the cations. These properties are particularly pronounced for [2-Sema]⁺.

Thus far, we have analyzed and discussed the capacitance curves on the basis of a model that considers only the formation of a double layer on a *bare* Pt surface. This includes a monotonic increase of the surface charge upon increasing the electrode potential relative to the PZC. In the next chapter, the non-monotonic surface charging because of Pt oxide formation and, to a lesser extent, due to a reorientation of adsorbed water molecules, will be taken into account.

3.2.2 Model2: Modified mean field model, non-monotonic surface charging (two/three $U_{
m PZC}$)

Model2 should be valid for the Pt/PIL interface if the following conditions are satisfied: (i) specific adsorption of the PIL ions should be negligible; (ii) sufficient surface water is present to produce PtO_x; and (iii) the oxide layer underneath the PIL ions is similar to that formed on Pt in aqueous solutions. As noted above, there may be a stronger interaction of the π electrons of [1-EIm]⁺ with the *bare* Pt surface, but in general, condition (i) seems to be fulfilled. PtO_x is even formed at the lowest water contents used in this work, i.e., 2-3 mol% of water, as evidenced by the CVs of [Dema][TfO] and [1-EIm][TfO] (see Fig. S1 and the inset pictures in Fig. 1). The CVs shown here and in previous works [5, 46, 67], particularly those of the acidic PILs [2-Sema][TfO] and [2-Sea][TfO], are very similar to the CVs obtained in Pt-electrodes in acidic aqueous solutions, even at bulk water contents as small as 10–20 mol%. This suggests that under these conditions, the oxide layers should be similar as well. On the other hand, the coverage of water molecules on the oxide surface should be lower in the PILs because of their much smaller bulk water content. This, in turn, should reduce the effect of the reorientation of the water molecules on the surface charging. It can be concluded that [2-Sema][TfO] with a sufficiently high amount of water is the electrolyte that best meets conditions (i) –(iii). For this reason, the simulations were carried out taking [2-Sema][TfO] with ≈20mol% of water as an example (see Fig. 7).

The principal course of the metal surface charge vs. the electrode potential adopted from Huang et al. is shown in the inset picture in Fig. 7a: Starting from H_{UPD} at U = 0 vs. Pd–H, the metal charge turns from negative to positive as the first PZC, $U_{PZC1} = 0.28$ V, is exceeded. A deviation from the linear increase in the metal charge towards lower values occurs as the surface oxidation starts. The increasingly negative charge of the oxide anions and, to a lesser extent, the corresponding reorientation of water molecules, leads to a second PZC, $U_{PZC2} = 0.8$ V, in which the surface turns from positive to negative charges. U_{PZC2} is similar to the value of ≈ 0.77 V vs. SHE calculated by Huang et al. [36] for an acid aqueous solution with pH = 1.2.

As with U_{PZC1} , U_{PZC2} was not experimentally-determined but set to a value that yields the best match of experimental and simulated capacitances in the potential range of Pt oxidation. If C_1 were to be free from pseudo-capacitances (due to specific ion adsorption and/or Faradaic currents), U_{PZC1} would equal the PZFC of the bare metal surface and U_{PZC2} that of the oxide surface. Note that with Model1, it is assumed that the oxidation of water, the chemisorption of oxygen species and the formation of Pt hydroxides and oxides cause pseudo-capacitances that limit a reasonable simulation of C_1 to the potential range between H_{UPD} and the onset of Pt oxide formation. With respect to potentials higher than the PtO_x onset potential, this differs with Model2, the simulations with which were based on the following assumptions:

- (a) The non-monotonic charging model of Huang et al. is also valid for ionic liquids with at least residual water (conditions (i)–(iii) are fulfilled).
- (b) The C_1 values derived from impedance spectra can be assigned to pure double layer effects, e.g., reorientation and redistribution of ions, without any amount of pseudocapacitances due to specific adsorption or Faradaic reactions.
- (c) The equations used for Model1 also apply to Model2. The only difference is that: (i) two or three potential ranges with different PZCs are separately simulated; and (ii) for the simulation around U_{PZC2} , γ_+ turns to γ_- and vice versa, because the cathodic branch corresponds to the positive surface charge and the anodic branch to the negative one (see Eq. S8).

The most critical issues relate to point 3. For example, the higher capacitance at U_{PZC2} (17.0 μ F/cm²) compared to U_{PZC1} (14.3 μ F/cm²) requires γ - <½ for the anodic branch of the simulation curve around U_{PZC1} (increase of C_1 !) but a larger γ - value >½ for the cathodic branch of the simulation curve around U_{PZC2} (decrease of C_1 !). Unfortunately, such large values of γ - cannot be reconciled with the current picture of the amount of free ions in ionic liquids. However, if we ignore this concerning fact, the inevitable result is a jump of γ in the transition region

between both curves. It appears unlikely that a gradual change in the coverage of oxidized species should lead to a jump in γ . Rather than a stepwise change, there will be a smooth transition between the γ values of different branches (the same also holds for the other parameters, namely α , X, ε , and \bar{c}).

Another issue concerns the non-monotonic, non-linear charging behavior in the potential range of ≈ 0.6 –0.9V. In general, a linear relationship between the free charge density of a metal (excluding specific adsorption), $\sigma_{\rm M}$, and $U-U_{\rm PZC}$ only exists if C_1 is independent of the potential. The latter is obviously not the case, *i.e.*, there is a non-linear potential dependence of $\sigma_{\rm M}$, regardless of whether or not the charging behavior is monotonic. This suggests that the eqs. S1–8 might also apply to Model2.

Future analytical solutions for the differential double layer capacitance should account for non-monotonic charging with at least two or three PZCs and, by using an interpolation function, for the transition between the different states of the Pt surface (e.g., bare \leftrightarrow oxidized \leftrightarrow passive). Moreover, the effect of water molecules on the electrode/PIL interface should be considered. This involves the potential-dependent amount of water, X, as well as the specific coverages and interactions of water on/with the different Pt surfaces, e.g., reorientation on the surface or incorporation into the oxide film. For example, the adaptation of Eq. S4 for different surface states would help avoid jumps in the amount of water, the dielectric constant, and the average ion concentration in the double layer. However, these refinements would form part of future analyses and are beyond the scope of this work.

As is shown in Fig. 7a, the simulation of the experimental C_1/U -curve gives good results, apart from the steep increase of C_1 between 1–1.2 V. The use of an additional PZC not only allows C_1 to be simulated above 0.9 V but also yields better matching of the hump of around 0.6 V, which is poorly simulated using Model1 (compare Fig. 3c). At potentials above 0.6 V, where it is assumed that the surface charging starts to deviate from the monotonic increase, the

transition from the bare to the oxidized Pt surface takes place. 'Oxidized' in this context refers to a coverage of oxide species smaller than one. As discussed above, modification and refinement of the equations used for Model2 should allow a smooth transition between the correlation factors and γ . values of the positive branch of the green curve (0.22/0.164) and the negative branch of the red curve (0.19/0.39). It is noteworthy that the simulated C_1/U -curve around U_{PZC2} (red curve) fits the experimental data reasonably well across a broad potential range from 0.45–1.6 V. The inverse charge distribution around U_{PZC2} (σ_M >0 for U< U_{PZC2} , σ_M <0 for U> U_{PZC2}) and the shape of the C_1/U -curve results in \approx 4 times higher γ . than γ + values (0.39 vs. 0.11). This result is not easy to understand and suggests that the compacity values obtained with equations that do not account for the properties of the oxidized Pt surface are still apparent values. Note that each of the curves is normalized to the respective experimental capacitance at the corresponding PZC, following Eq. S1. Without normalization, there would be no coincidence of green and red curves around 0.75 V.

The model of Huang et al. predicts that above 0.8 V, a further increase in potential leads again to an increase in the metal charge. At sufficiently high potentials, the overall charge should turn again from negative to positive values. Although not explicitly shown in Huang's article, the appearance of a third PZC at high potentials can be expected. However, to the best of our knowledge, the third PZC has not been experimentally-verified thus far. We tentatively chose the potential at the bend in the passive region, i.e., $U_{PZC3} = 1.36 \text{ V}$. As can be seen in Fig. 7b, the analysis of C_1 with three PZCs yields a better simulation, particularly in the passive region. In the potential range around 1.04 V, where C_1 steeply increases, there must be a transition between the clearly different γ_+ (and σ) values of the red and blue simulation curves. Analogous to the change from the blank to the oxidized Pt surface, this corresponds to a transition from oxidized to passivated metal. With respect to the former, the question arises as

to whether Eq. S2 is valid for the passive region. If not, apparent α and γ values around U_{PZC3} would be obtained.

Whereas Frumkin and others proved the existence of more than one PZC on Pt metals in aqueous solutions, experimental evidence of one or even two additional PZCs on the metal (Pt) oxide surface in contact with ionic liquids is still lacking. In any case, the existence of a non-monotonic charging of the Pt surface will result in a distinct change in the double layer structure: Contrary to monotonic charging, where relatively high positive charges would be obtained on the oxidized Pt surface, moderate surface charges with alternating signs must result if non-monotonic charging takes place. In the former case, an excess of anions in the double layer and particularly in the innermost ion layer is expected. In the latter one, the sign of the surface charge changes up to three times across the potential range investigated, accompanied by a change in the dominating ion species in the innermost layer and the sequence of alternating anion and cation layers. Because of the moderate surface charges, the overscreening effect will be important in the entire potential range, *i.e.*, also on the oxidized/passivated Pt surface at higher electrode potentials. Conversely, the crowding effect that occurs at high surface charges [22] should play a minor role in the potential range investigated here.

In summary, the *qualitative* results of the non-monotonic charging model of Huang et al. [36] seem to be valid for Pt electrodes in ionic liquid/water mixtures as well. However, the difficult-to-interpret γ values in the oxidized and passive regions and jumps of γ in the transition regions between the simulated curves suggest the development of a (mean field) model that takes into account different states of the Pt surface. The simulations of the experimental results presented so far rely on the analysis of the high-frequency capacitance C_1 that represents 'true' double layer behavior, either in a relatively narrow potential range between H_{UPD} and Pt oxidation (model1) or at potentials higher than the H_{UPD} region (Model2). In the next chapter, we present the experimental results of the mid-frequency, pseudo-capacitance C_2 associated

with Faradaic processes. A special emphasis is placed on the effect of the cations and water molecules on Pt oxidation.

3.3 Mid-frequency capacitance, C_2

A previous study on the differential double layer capacitance in the interface of Pt and mixtures of [2-Sema][TfO] and water revealed that the mid-frequency (m.f.) capacitance, C_2 , is associated with pseudo-capacitive processes [5]. This was apparent from a steep increase in C_2 in the H_{UPD} region and a pronounced peak that appeared during the formation of a passive layer. Beneath specific adsorption and Faradaic processes, another reason for the occurrence of m.f. capacitances is a reconstruction of the metal surface, as reported by Drüschler et al. [12].

The potential-dependent m.f. capacitances for different water contents and temperatures are shown in Fig. 8 and Fig. 9. As expected, the three PILs show a steep increase in C_2 in the H_{UPD} region (U = 0–0.3 V). Surprisingly, a more or less pronounced peak (here denoted as peak1) was observed in the double layer region for [Dema][TfO] (around 0.7V) and [2-Sema][TfO] (around 0.5V), whereas [1-EIm][TfO] exhibited only occasional or small effects. Because of the latter and the erratic fluctuations of the peak area at different water contents for [Dema][TfO], the dependence of the peak area on the water content and temperature was analyzed for the example of [2-Sema][TfO]. Note that in our previous study, C_2 was only evaluated for [2-Sema][TfO] with 38 mol% (3.7 wt%) water and 90 °C and the shoulder at 0.5 V was attributed to an inaccuracy of the fitting process and not discussed [5]. However, this study reveals that there is a peak or even a shoulder at about 0.5 V across the entire range of the water content and temperature investigated.

As is shown in Fig. S7 and Fig. S8, there is virtually no impact of water content, whereas there is a roughly linear correlation between the temperature and peak area. This suggests that peak1 can be attributed to a thermally-activated, slow process that does not involve water. Possible effects that would be consistent with such a process have been described in the literature, including reconstruction of the electrode surface [25], a strong metal-anion interaction [12] and the associated reorientation or ad-/desorption of PIL ions [18]. What is common to all of these—slow—processes is that they occur on the metal surface or in the innermost layer. Utilizing MD simulations with (water-free) [BMIm][PF₆] on Au(111), Voroshylova et al. recently identified up to four capacitive peaks across a wide range of potentials, even though they did not distinguish between slow and fast capacitive processes [68]. However, none of these peaks arises at potentials close to 0.5 V and it is therefore questionable whether one of them corresponds to peak 1. The closest capacitance peak arises at 1.2 V and is due to the transition of the double layer with an innermost layer that consists of an equal number of anions and cations (PZC) to one with only anions that forms at a critical, positive charge [68]. Overall, a reliable identification of the process underlying peak1 is not possible without additional, structural information gained from surface-sensitive methods such as AFM, STM, or SNIFTIRS.

Conversely, the peaks and/or the increase in capacitance at potentials higher than 0.9–1.0 V can be unequivocally attributed to Pt oxidation and/or the OER. This is evident from the comparison of the C_2/U -curves and the anodic scans of the CVs and is illustrated in Fig. S9 for the example of 90 °C and \approx 20 mol% of water. The CVs show that, unlike [2-Sema][TfO], the Pt oxides of [1-EIm][TfO] and [Dema][TfO] do not form passive layers. This is proven by the pronounced increase in current density at the onset of OER and the relatively small oxide reduction peak in the reverse scan. In turn, this leads to fundamentally different C_2/U -curves in the Pt oxidation region: Whereas [2-Sema][TfO] shows only a single capacitance peak at \approx 1.1

V (denoted here as peak2), a hump at around 1.1–1.2 V and a strong increase in C_2 at potentials higher than 1.3 V is observed for [1-EIm][TfO] and [Dema][TfO]. Surprisingly, the hump tends to decrease and shift to higher potentials with increasing water content. This might be explained by an oxidation process that takes place *via* different mechanisms: at low water contents, the hump is mainly due to an oxidation mechanism that needs only one instead of three water molecules per Pt atom but involves the (neutral) cation precursor as a proton acceptor [5] (Eq. 3a):

$$Pt_{surf} + 2B(1) + H_2O(1) \rightleftharpoons (Pt^{2+} - O^{2-})_{3D \ lattice} + 2BH^+(1) + 2e^-$$
 (3a)

$$Pt_{surf} + 3H_2O(1) \rightleftharpoons (Pt^{2+}-O^{2-})_{3D \ lattice} + 2H_3O^+(1) + 2e^-$$
 (3b)

At higher water contents, the common oxidation mechanism prevails, involving three water molecules per Pt atom (Eq. 3b). Although the onset potential of the common mechanism is somewhat higher, it shifts in the negative direction if the water content increases. It is therefore not surprising that the—shrinking—hump finally disappears at $x_{H2O}>30$ mol%, probably masked by the steep increase in the capacitance that occurs at increasingly lower potentials.

As Pt oxidation is a thermally-activated process, the CV current density, as well as the humps and peak2, increase with temperature (see Fig. 9). As can be seen in Fig. S7, the area of peak2 increases almost linearly with rising water content. This suggests that Pt oxidation in the presence of [2-Sema][TfO] proceeds mainly via the common oxidation mechanism (Eq. 3b), resulting in the formation of a passive film. This differs from the oxide films formed in the presence of [1-EIm][TfO] and [Dema][TfO], probably with the involvement of the cation precursors that even allow OER at potentials above 1.2 V. In any case, the type of cation has an impact on the oxide growth. This is not that surprising, as even in acidic aqueous solutions, where the anions tend to desorb during oxide formation, an indirect influence of anions *via* a change in the electrical field in the double layer and the oxide layer on the oxide formation kinetics has been reported [69]. If anions may—indirectly—effect the oxide growth, this will

be especially true for the cations; that is, the predominant ion species on a negatively-charged oxide surface (see the non-monotonic charging model). The question of how exactly the different cations would affect the electrical field cannot be answered on the basis of what has been discussed so far and should be subjected to further investigation. Another, straightforward explanation lies in the assumed smaller surface coverage of water in the presence of [1-EIm][TfO] and [Dema][TfO] compared to [2-Sema][TfO] (see the discussion above). This might result in the formation of thin oxide layers that have only a limited passivation effect.

In summary, the pseudo-capacitance of the Pt/[2-Sema][TfO] interface shows a distinctly different behavior compared to those obtained with [1-EIm][TfO] and [Dema][TfO]. This is especially true for oxidized Pt and is due to the fact that only [2-Sema][TfO] forms passive layers at bulk water contents of up to 50 mol%, similar to those observed in aqueous solutions. Different mechanisms of Pt oxide formation may be a possible reason for this, but still need to be proven.

4. Conclusions

The general insights from the presented analysis of the experimental data on the high-frequency double layer and mid-frequency pseudo-double layer capacitances of the Pt/protic ionic liquid interface obtained in this work are as follows:

- When using a mean field model that accounts for the presence of water, the introduction
 of short range correlations of ions is necessary. Then, the double layer capacitance of
 very different water-containing protic ionic liquids with respect to their cation properties
 such as acidity, structure, and hydrogen bonding ability can be simulated fairly well.
- Matching the results of the theory to the obtained experimental data provided us with
 useful hints regarding a number of interfacial and bulk properties, including: (i) the
 modes of charging of the Pt electrode; (ii) the dominating ionic species in the innermost

- layer; (iii) the orientation and surface concentration of the water; (iv) the short-range interionic forces; and (v) the degree of ion clustering.
- Although species involved in electrode reactions are part of the double layer, electrolyte properties such as cation acidity do not necessarily have the same effect on both electrode kinetics and double layer properties: in contrast to its influence on the oxygen reduction reaction, the acidity of the cation has no direct effect on the double layer properties.
- In future simulations, non-monotonic charging on oxidized or even passive metal surfaces involving up to three potential of zero charges may need to be considered because, particularly at higher potentials, this may have a dramatic effect on the potential-dependent surface charge and so the double layer structure and properties.
- The correlation between the pseudo-capacitance *vs.* potential curves and the cyclic voltammograms provides valuable hints regarding the structure and properties of oxide film(s) formed in the presence of ionic liquids. However, it remains an open question as to why, depending on the type of cation, passive films are formed or not, and how the cation affects oxide growth and film formation.

Some results thus presented in this work raise further questions that cannot be answered solely using electrochemical methods, but may require additional information from surface-sensitive and spectroscopic methods such as AFM, STM, or SNIFTIRS, combined with molecular dynamics. In particular, this concerns the existence of a third PZC or the influence of the cation on the oxide film formation. Moreover, the development of an analytical solution based on a modified charging model that takes into account the special structure and properties of the metal/ionic liquid interface would be desirable.

The analysis of the double layer capacitance by a mean field model as presented here has its own limitations. It captures the effects of ion crowding and the balance between free and

clustered ion states. Implicitly, it incorporates cracking of ion clusters in the double layer. However, it does not consider explicitly the effects of overscreening of ions in the double layer that are expected to be pronounced at small electrode polarizations. The latter have already been predicted at ideally flat, sharp boundary electrodes, but are expected to get substantially suppressed at even atomically rough electrodes.

It is still a long way to understand how the described picture could affect electrochemical kinetics of even most elementary processes at metal catalyst/ionic liquid interfaces and how the driving force for such reactions would depend on electrode potential. Once that was made clear, these concepts might help to formulate measures for boosting electrochemical reactions in future generations of fuel cells, electrolyzers and batteries that use ionic liquid electrolytes.

Acknowledgements

We gratefully acknowledge the valuable insights regarding the non-monotonic charging model given by Professor M. Eikerling (IEK-13). We are also grateful to K. Klafki for her assistance with the Karl–Fischer titration method. We are also obliged to C. Wood for proofreading the manuscript.

References

- [1] G. Feng, X. Jiang, R. Qiao, A. A. Kornyshev, ACS Nano 2014, 8, 11685.
- [2] K. Motobayashi, M. Osawa, Electrochem. Commun. 2016, 65, 14.
- [3] Y. Zhong, J. Yan, M. Li, L. Chen, B. Mao, ChemElectroChem 2016, 3, 2221.

- [4] J. Friedl, I. I. E. Markovits, M. Herpich, G. Feng, A. A. Kornyshev, U. Stimming, ChemElectroChem 2017, 4, 216.
- [5] K. Wippermann, J. Giffin, S. Kuhri, W. Lehnert, C. Korte, *Phys. Chem. Chem. Phys.* **2017**, 19, 24706.
- [6] S. Bi, R. Wang, S. Liu, J. Yan, B. Mao, A. A. Kornyshev, G. Feng, *Nature Communications* **2018**, *9*, 5222.
- [7] A. Kemna, B. Braunschweig, *The Journal of Physical Chemistry Letters* **2020**, *11*, 7116.
- [8] Y. A. Budkov, A. L. Kolesnikov, Z. A. H. Goodwin, M. G. Kiselev, A. A. Kornyshev, *Electrochim. Acta* **2018**, 284, 346.
- [9] M. A. B. H. Susan, M. Yoo, H. Nakamoto, M. Watanabe, Chem. Lett. 2003, 32, 836.
- [10] A. Noda, M. A. B. H. Susan, K. Kudo, S. Mitsushima, K. Hayamizu, M. Watanabe, *J. Phys. Chem. B* **2003**, *107*, 4024.
- [11] W. Böld, M. Breiter, *Electrochim. Acta* **1961**, *5*, 145.
- [12] M. Drüschler, B. Huber, B. Roling, J. Phys. Chem. C 2011, 115, 6802.
- [13] A. A. Kornyshev, J. Phys. Chem. B 2007, 111, 5545.
- [14] G. Feng, M. Chen, S. Bi, Z. A. H. Goodwin, E. B. Postnikov, N. Brilliantov, M. Urbakh, A. A. Kornyshev, *Physical Review X* **2019**, *9*, 021024.
- [15] Y. Zhang, T. Ye, M. Chen, Z. A. H. Goodwin, G. Feng, J. Huang, A. A. Kornyshev, ENERGY & ENVIRONMENTAL MATERIALS 2020, 3, 414.
- [16] Z. A. H. Goodwin, A. A. Kornyshev, *Electrochim. Acta* **2022**, *434*, 141163.
- [17] M. T. Alam, M. M. Islam, T. Okajima, T. Ohsaka, J. Phys. Chem. C 2008, 112, 16600.
- [18] M. M. Islam, M. T. Alam, T. Ohsaka, J. Phys. Chem. C 2008, 112, 16568.

- [19] V. Lockett, R. Sedev, J. Ralston, M. Horne, T. Rodopoulos, *J. Phys. Chem. C* **2008**, *112*, 7486.
- [20] M. V. Fedorov, A. A. Kornyshev, *Electrochim. Acta* **2008**, *53*, 6835.
- [21] M. V. Fedorov, A. A. Kornyshev, *J Phys Chem B* **2008**, *112*, 11868.
- [22] M. Z. Bazant, B. D. Storey, A. A. Kornyshev, *Phys. Rev. Lett.* **2011**, *106*, 046102/1.
- [23] R. Atkin, N. Borisenko, M. Druschler, F. Endres, R. Hayes, B. Huber, B. Roling, *J. Mol. Liq.* **2014**, *192*, 44.
- [24] F. Endres, N. Borisenko, S. Zein El Abedin, R. Hayes, R. Atkin, *Faraday Discuss.* **2012**, *154*, 221.
- [25] R. Atkin, N. Borisenko, M. Druschler, S. Z. El Abedin, F. Endres, R. Hayes, B. Huber, B. Roling, *Phys. Chem. Chem. Phys.* **2011**, *13*, 6849.
- [26] R. Hayes, N. Borisenko, M. K. Tam, P. C. Howlett, F. Endres, R. Atkin, J. Phys. Chem. C 2011, 115, 6855.
- [27] C. Rodenbücher, Y. Chen, K. Wippermann, P. M. Kowalski, M. Giesen, D. Mayer, F. Hausen, C. Korte, *International Journal of Molecular Sciences* **2021**, 22, 12653.
- [28] Y. Zhong, J. Yan, M. Li, L. Chen, B. Mao, *ChemElectroChem* **2016**, *3*, 2221.
- [29] Y.-X. Zhong, J.-W. Yan, M.-G. Li, X. Zhang, D.-W. He, B.-W. Mao, J. Am. Chem. Soc. 2014, 136, 14682.
- [30] S. Perkin, Phys. Chem. Chem. Phys. 2012, 14, 5052.
- [31] A. Sheehan, L. A. Jurado, S. N. Ramakrishna, A. Arcifa, A. Rossi, N. D. Spencer, R. M. Espinosa-Marzal, *Nanoscale* **2016**, *8*, 4094.
- [32] M. Mezger, R. Roth, H. Schröder, P. Reichert, D. Pontoni, H. Reichert, J. Chem. Phys. 2015, 142, 164707.

- [33] Z. A. H. Goodwin, G. Feng, A. A. Kornyshev, *Electrochim. Acta* **2017**, 225, 190.
- [34] A. N. Frumkin, O. A. Petrii, *Electrochim. Acta* **1975**, 20, 347.
- [35] A. Shlygin, A. Frumkin, V. Medvedovsky, Acta Physicochim. URSS 1936, 4, 911.
- [36] J. Huang, A. Malek, J. Zhang, M. H. Eikerling, J. Phys. Chem. C 2016, 120, 13587.
- [37] K. Wippermann, Y. Suo, C. Korte, J. Electrochem. Soc. 2020, 167, 046511.
- [38] K. Wippermann, Y. Suo, C. Korte, J. Phys. Chem. C 2021.
- [39] K. Wippermann, J. Giffin, C. Korte, J. Electrochem. Soc. 2018, 165, H263.
- [40] K. Wippermann, J. Wackerl, W. Lehnert, B. Huber, C. Korte, *J. Electrochem. Soc.* **2016**, *163*, F25.
- [41] C. G. Malmberg, A. A. Maryott, *Journal of Research of the National Bureau of Standards* **1956**, *56*, 1.
- [42] H. Weingärtner, Journal of Molecular Liquids 2014, 192, 185.
- [43] H. Weingärtner, A. Knocks, W. Schrader, U. Kaatze, *Journal of Physical Chemistry A* **2001**, *105*, 8646.
- [44] M.-M. Huang, Y. Jiang, P. Sasisanker, G. W. Driver, H. Weingärtner, *Journal of Chemical & Engineering Data* **2011**, *56*, 1494.
- [45] J. Hunger, A. Stoppa, S. Schrödle, G. Hefter, R. Buchner, ChemPhysChem 2009, 10, 723.
- [46] K. Wippermann, J. Giffin, C. Korte, J. Electrochem. Soc. 2018, 165, H263.
- [47] M. W. Breiter, Journal of Electroanalytical Chemistry (1959) 1964, 7, 38.
- [48] T. Köddermann, C. Wertz, A. Heintz, R. Ludwig, ChemPhysChem 2006, 7, 1944.
- [49] Y. Zhang, E. J. Maginn, *The Journal of Physical Chemistry Letters* **2015**, *6*, 700.

- [50] B. Kirchner, F. Malberg, D. S. Firaha, O. Hollóczki, *Journal of Physics: Condensed Matter* **2015**, *27*, 463002.
- [51] X. Zhong, Z. Fan, Z. Liu, D. Cao, J. Phys. Chem. B 2012, 116, 3249.
- [52] T. Iwasita, X. Xia, J. Electroanal. Chem. 1996, 411, 95.
- [53] V. Climent, N. Garcia-Araez, E. Herrero, J. Feliu, Russ. J. Electrochem. 2006, 42, 1145.
- [54] Q.-S. Chen, J. Solla-Gullon, S.-G. Sun, J. M. Feliu, *Electrochim. Acta* 2010, 55, 7982.
- [55] A. Ejigu, D. A. Walsh, J. Phys. Chem. C 2014, 118, 7414.
- [56] Y. Uematsu, R. R. Netz, D. J. Bonthuis, *Journal of Physics: Condensed Matter* **2018**, *30*, 064002.
- [57] H. A. Every, ECS Proceedings Volumes 2004, 2004-21, 277.
- [58] R. Eschenbacher, C. Schuschke, H. Bühlmeyer, N. Taccardi, P. Wasserscheid, T. Bauer,T. Xu, J. Libuda, *The Journal of Physical Chemistry Letters* 2021, 12, 10079.
- [59] S. Trasatti, Journal of Electroanalytical Chemistry and Interfacial Electrochemistry 1971, 33, 351.
- [60] A. R. Porter, S. Y. Liem, P. L. A. Popelier, Phys. Chem. Chem. Phys. 2008, 10, 4240.
- [61] P. D'Angelo, A. Zitolo, G. Aquilanti, V. Migliorati, J. Phys. Chem. B 2013, 117, 12516.
- [62] Y. Suo, Characterization of proton conducting ionic liquids as alternative electrolytes for applications > 100°C in high temperature polymer electrolyte fuel cells, in, RWTH Aachen University, Jülich, 2022.
- [63] Y. Suo, H. Hou, J. Lin, Y. Chen, C. Liu, C. Wang, P. S. Schulz, K. Wippermann, C. Korte, J. Phys. Chem. C 2021.
- [64] M. V. Fedorov, A. A. Kornyshev, Chem. Rev. (Washington, DC, U. S.) 2014, 114, 2978.

- [65] L. Zhang, Z. Zhang, W.-L. Yuan, N. Zhao, Q.-H. Zhu, L. He, G.-H. Tao, ChemPhysChem 2019, 20, 3259.
- [66] J. Lin, L. Wang, T. Zinkevich, S. Indris, Y. Suo, C. Korte, Phys. Chem. Chem. Phys. 2019.
- [67] K. Wippermann, J. Wackerl, W. Lehnert, B. Huber, C. Korte, *J. Electrochem. Soc.* **2016**, *163*, F25.
- [68] I. V. Voroshylova, H. Ers, V. Koverga, B. Docampo-Álvarez, P. Pikma, V. B. Ivaništšev,
 M. N. D. S. Cordeiro, *Electrochim. Acta* 2021, 379, 138148.
- [69] Y. Furuya, T. Mashio, A. Ohma, N. Dale, K. Oshihara, G. Jerkiewicz, J. Chem. Phys. 2014, 141, 164705/1.

Figure captions:

Fig. 1: CCP plots for three selected potentials representing different potential regimes (compare CVs in the inset pictures), $x_{\rm H2O} \approx 20$ mol%, T = 70 °C, f = 1 Hz-100 kHz: (a) [Dema][TfO]; (b) [1-EIm][TfO]; and (c) [2-Sema][TfO].

Fig. 2: Simulation of high-frequency capacitance C_1 vs. potential by Model1, variation of water content, T = 90 °C: (a) comparison of the 3 PILs, example of $x_{\rm H2O} \approx 30$ mol%; (b) [Dema][TfO]; (c) [1-EIm][TfO]; and (d) [2-Sema][TfO].

Fig. 3: Simulation of high-frequency capacitance C_1 vs. potential by Model1, variation of temperature, $x_{\rm H2O} \approx 20$ mol%: (a) comparison of the 3 PILs, example of T = 90 °C; (b) [Dema][TfO]; (c) [1-EIm][TfO]; and (d) [2-Sema][TfO].

Fig. 4: Correlation factor α vs. temperature (a) and water content (b); data obtained from the simulations shown in Fig. 2 and 3.

Fig. 5: (a) Compacity factor γ at PZC, γ_{PZC} , and the difference of repulsion and attraction forces at PZC, $(a-b)_{PZC}$, vs. temperature, example of ≈ 20 mol% H_2O ; (c) γ_{PZC} and $(a-b)_{PZC}$ vs water content, example of 90 °C; (b) and (d): inverse values of γ_{PZC} and $(a-b)_{PZC}$ vs temperature and water content; data obtained from the simulations shown in Fig. 2 and 3.

Fig. 6: Compacity values of the anions and cations, γ_{-} and γ_{+} , as a function of temperature (a) and water content (b); data obtained from the simulations shown in Fig. 2 and 3.

Fig. 7: Simulation of high-frequency capacitance C_1 vs. potential by Model2, example of [2-Sema][TfO] at 90 °C and 21.4 mol% of water; the inset picture shows the sketch of a possible, non-monotonic charging behavior adopted from Huang et al. [36]; (a) two PZCs; and (b) three PZCs.

Fig. 8: Simulation of mid-frequency capacitance C_2 vs. potential by Model1, variation of water content, T = 90 °C; (a) [Dema][TfO]; (b) [1-EIm][TfO]; and (c) [2-Sema][TfO].

Fig. 9: Simulation of mid-frequency capacitance C_2 vs. potential by Model1, variation of temperature, $x_{\rm H2O} \approx 20$ mol%: (a) [Dema][TfO]; (b) [1-EIm][TfO]; and (c) [2-Sema][TfO].

Figure captions for the Supplementary Data:

Fig. S1: Cyclic voltammograms (each 30^{th} of 30 cycles) on Pt under a nitrogen atmosphere, dU/dt=100 mV/s; variation of water content, T=90 °C: (a) [Dema][TfO]; (b) [1-EIm][TfO]; and (c) [2-Sema][TfO].

Fig. S2: Cyclic voltammograms (each 30^{th} of 30 cycles) of Pt under a nitrogen atmosphere, dU/dt=100mV/s; variation of temperature, $x_{H2O} \approx 20 \text{ mol}\%$: (a) [Dema][TfO]; (b) [1-EIm][TfO]; and (c) [2-Sema][TfO].

Fig. S3: Sensitivity analysis: effect of the chosen dielectric constant of the ionic liquids on parameters α and γ , example of [2-Sema][TfO] with \approx 50 mol% H₂O at 90 °C: (a) simulated C_1/U curves for $\epsilon_{\rm IL}$ = 10-60; (b) α and γ vs. $\epsilon_{\rm IL}$.

Fig. S4: Sensitivity analysis: effect of the chosen factor f_x of the water content on parameters α and γ , example of [2-Sema][TfO] with \approx 50 mol% H₂O at 90 °C: (a) simulated C_1/U curves for f_x = 0.1-3; (b) α and γ vs. f_x .

Fig. S5: Compacity factor γ vs. temperature, example of \approx 20 mol% H₂O: (a) [Dema][TfO]; (b) [1-EIm][TfO]; (c) [2-Sema][TfO]; data obtained from the simulations shown in Fig. 2 and 3.

Fig. S6: Compacity factor γ vs. water content, example of 90 °C: (a) [Dema][TfO]; (b) [1-EIm][TfO]; and (c) [2-Sema][TfO]; data obtained from the simulations shown in Fig. 2 and 3.

Fig. S7: Area of the peaks of the mid-frequency capacitance vs. water content; data evaluated from peak integration of the C_2 /U curves shown in Fig. 8.

Fig. S8: Area of the peaks of the mid-frequency capacitance vs. temperature, data evaluated from the peak integration of the C_2 /U curves shown in Fig. 9.

Fig. S9: Comparison of C_2/U curves and anodic scans of CVs, example of 90 °C and \approx 20 mol% of water: (a) [Dema][TfO]; (b) [1-EIm][TfO]; and (c) [2-Sema][TfO].

Table captions:

Table 1. Overview of structural data and electrochemical parameters derived from the analysis of the differential double layer capacitance; comparison of three PILs with different cations; values highlighted in green: order of cation acidity; values highlighted in blue: clearly different value of the acidic [2-Sema][TfO] compared to the less acidic PILs.

Table captions for the Supplementary Data:

Table S1. Terms used for the fit function of the WinFit 3.5 software, based on the empirical Cole–Cole type equation proposed by Drüschler et al. [12].

Fig.1

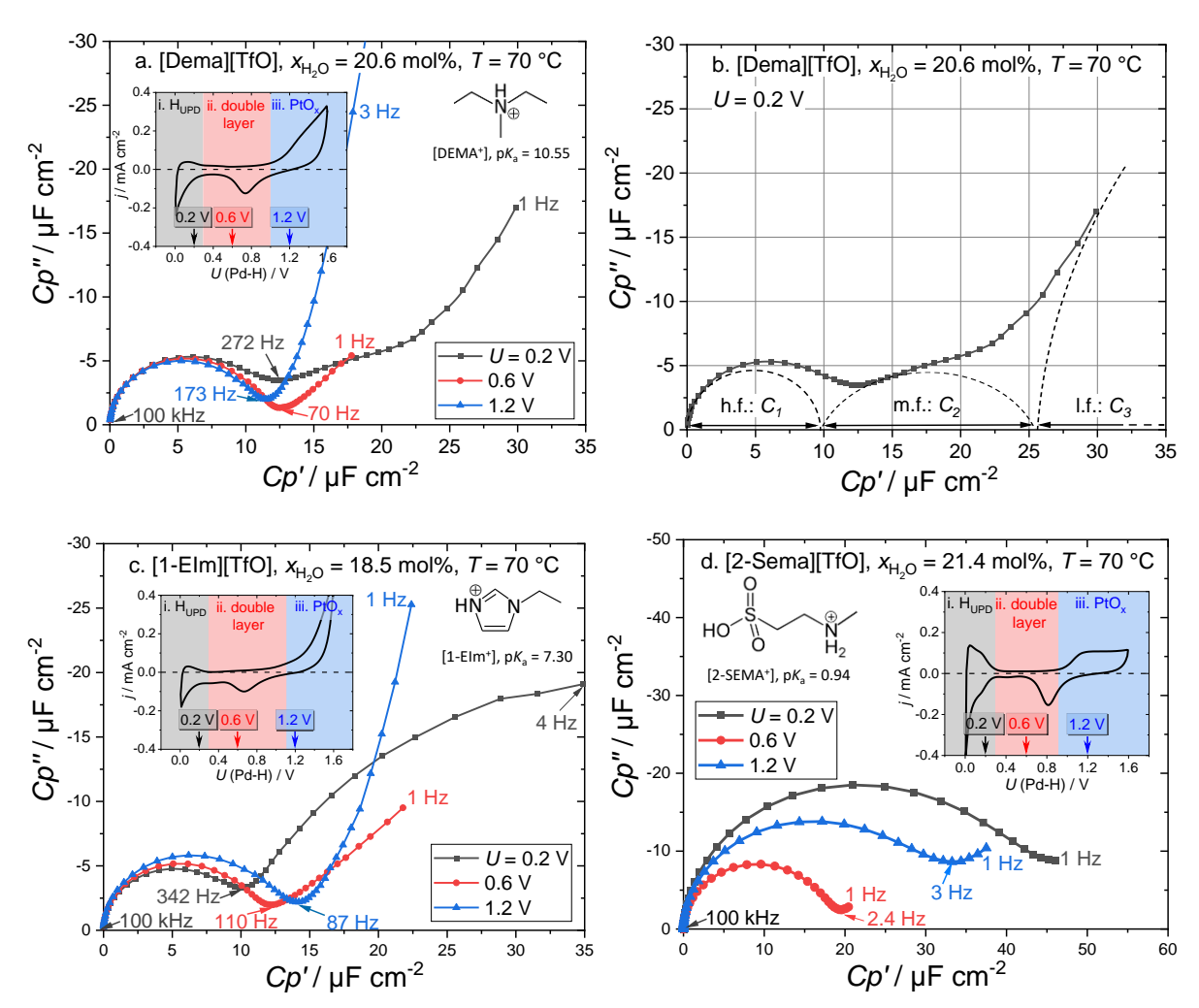


Fig.2

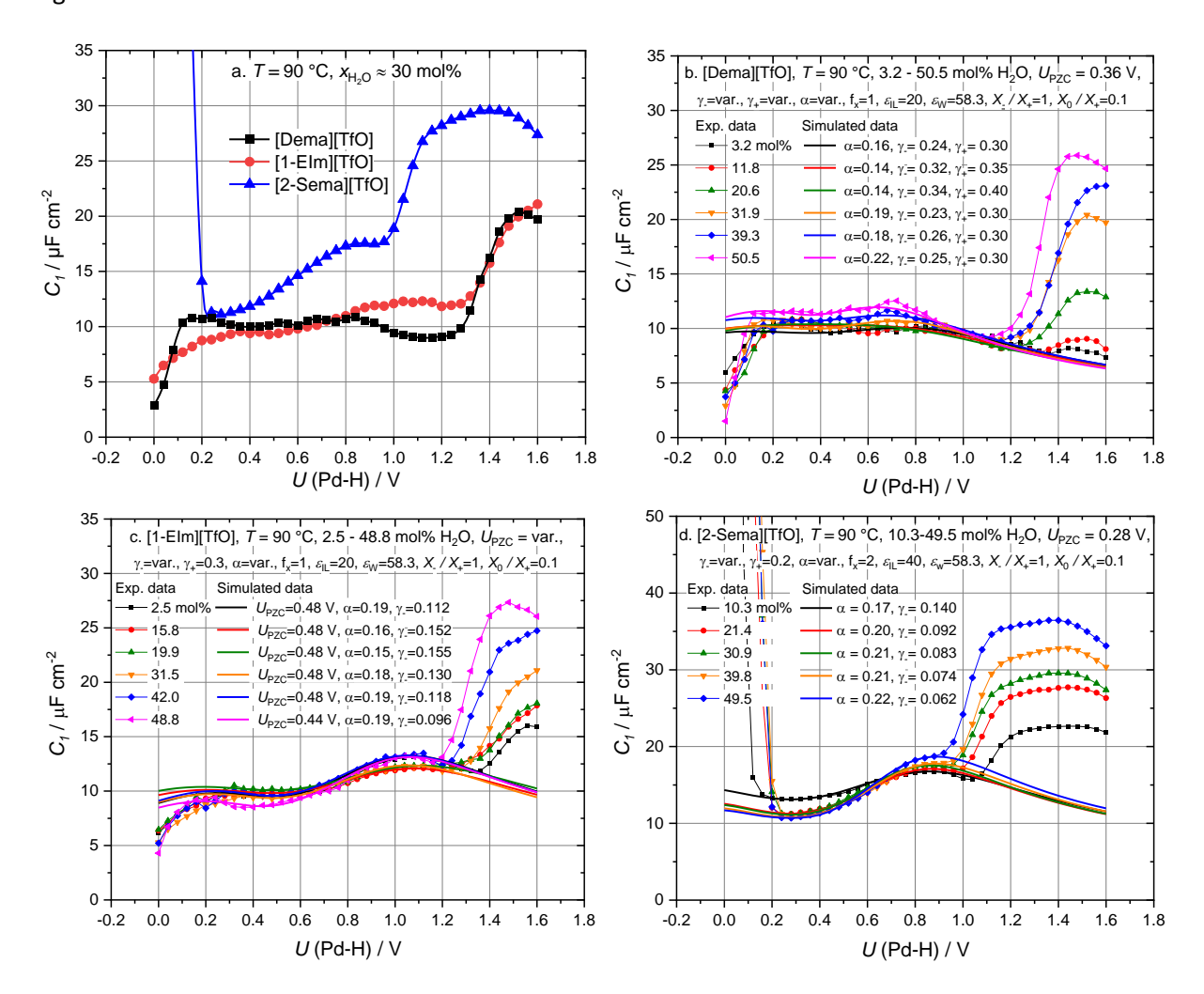


Fig.3

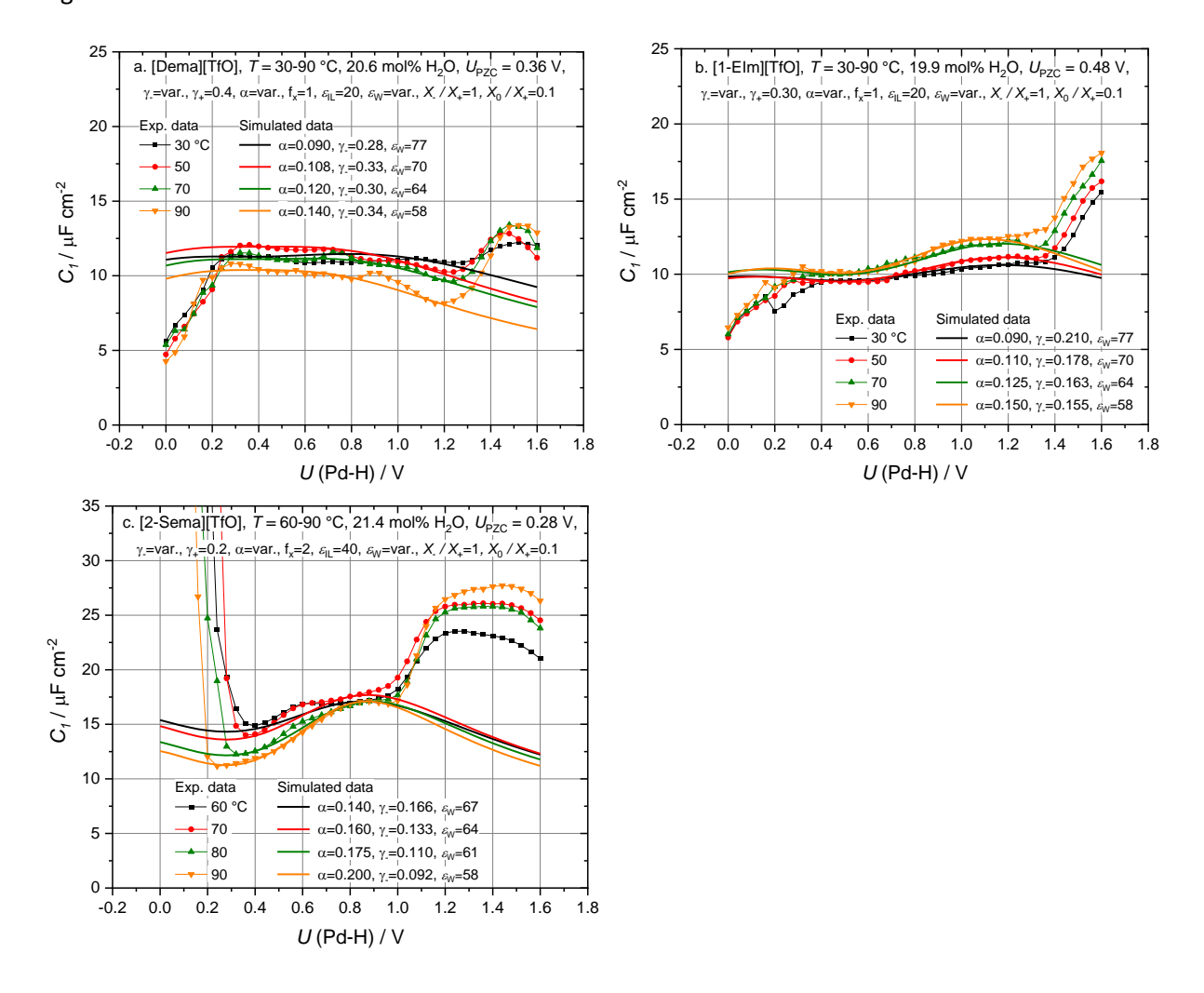


Fig.4

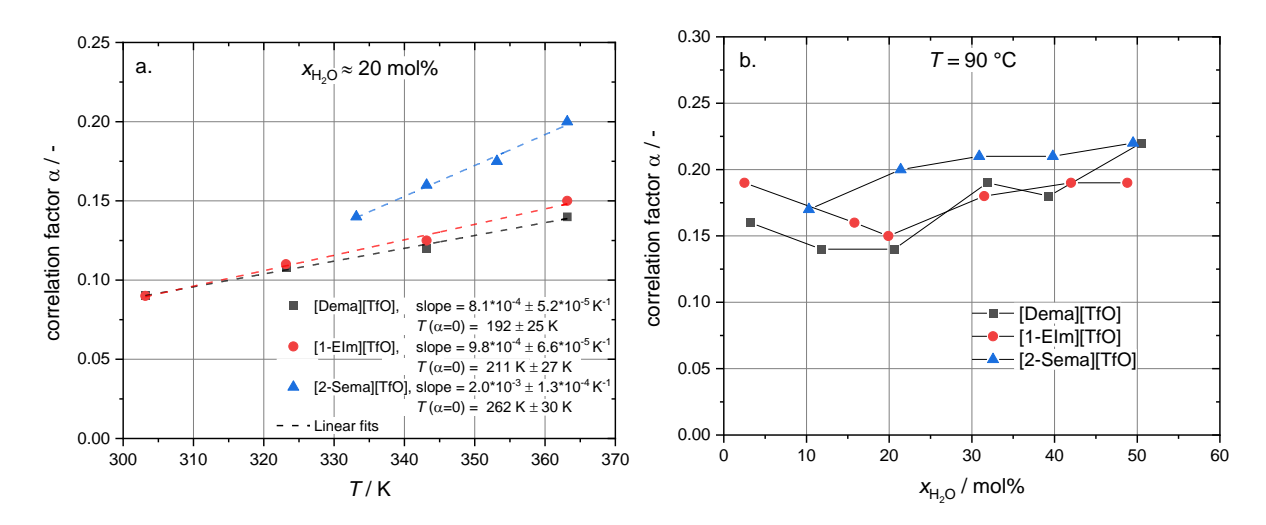


Fig.5

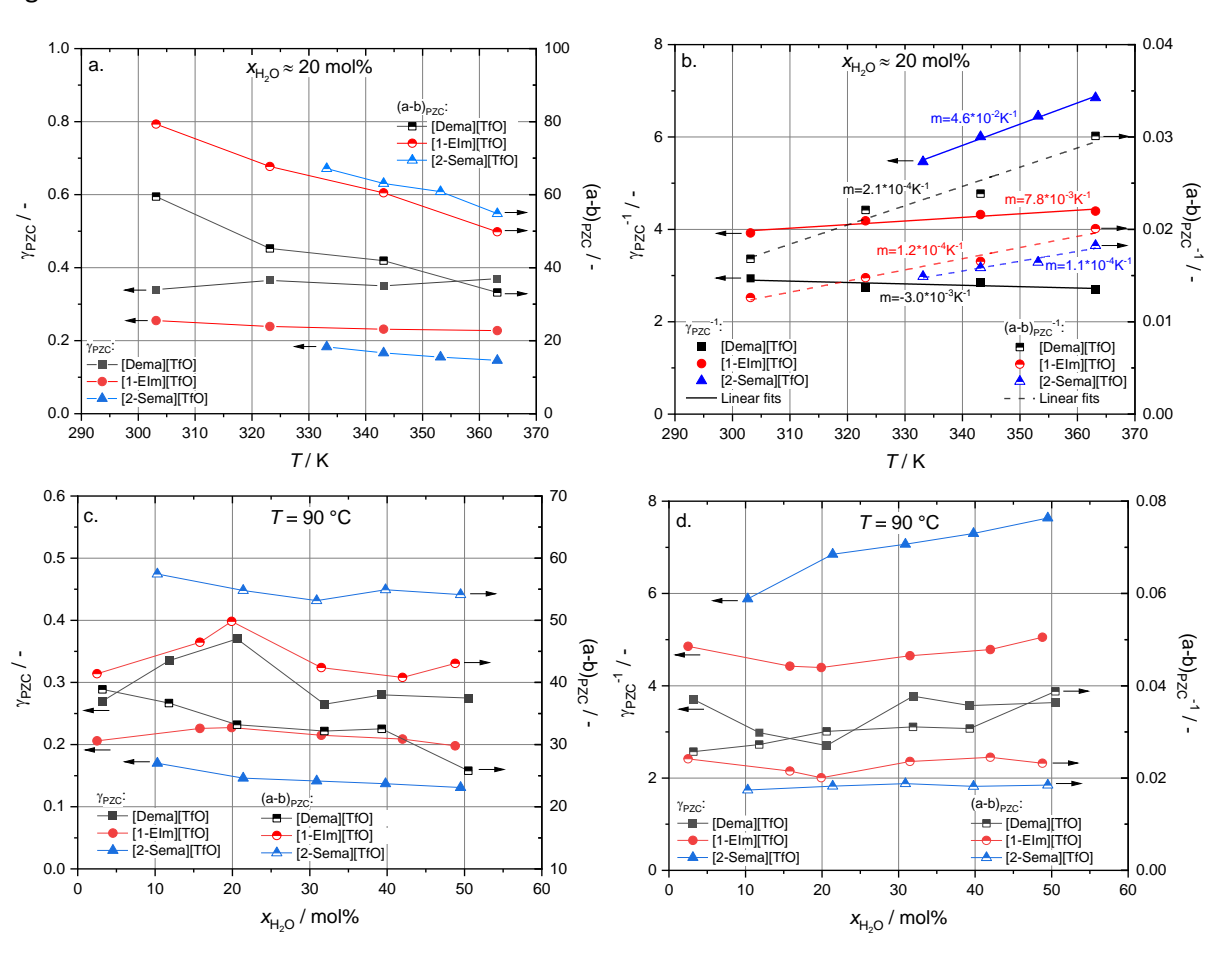


Fig.6

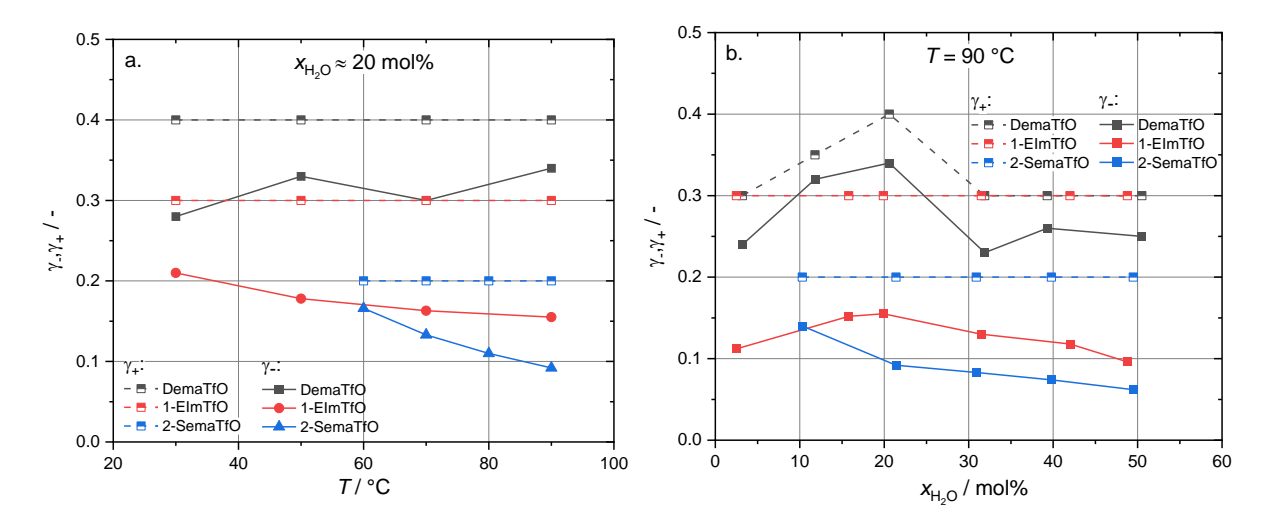


Fig.7

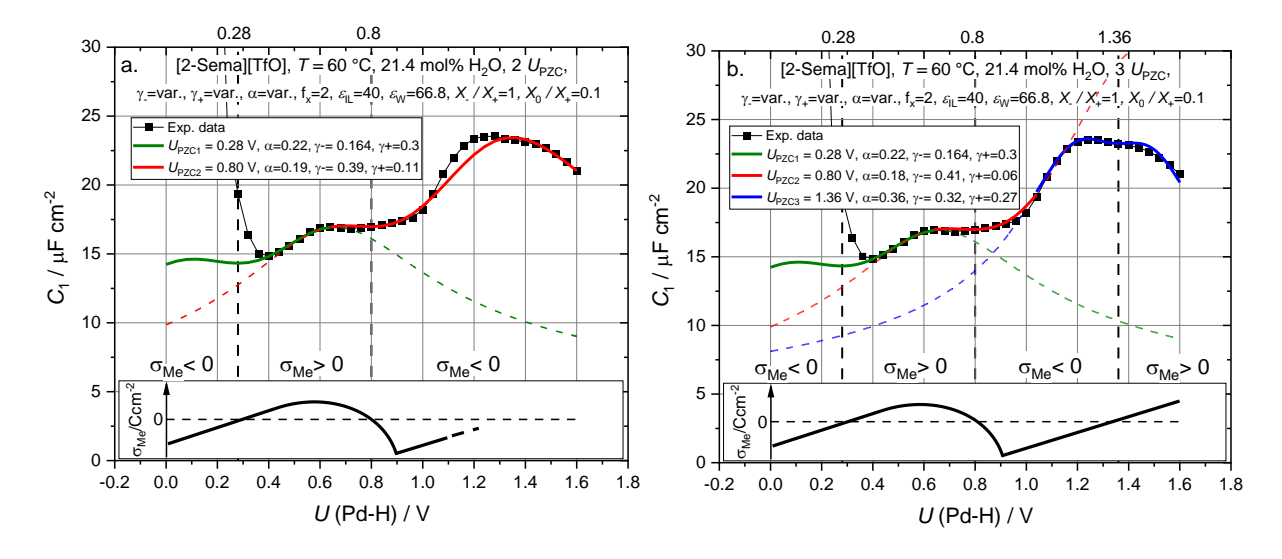


Fig.8

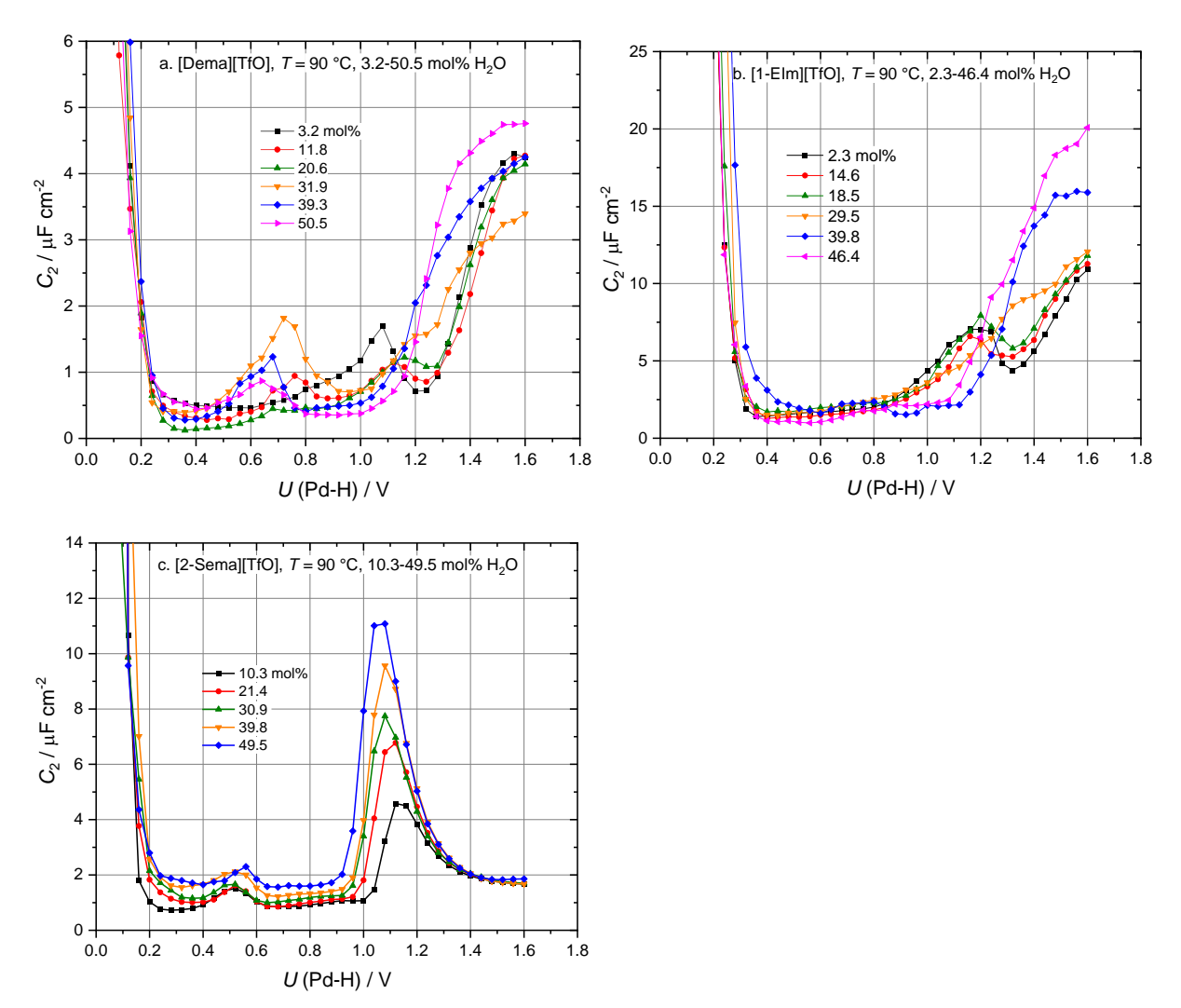


Fig.9

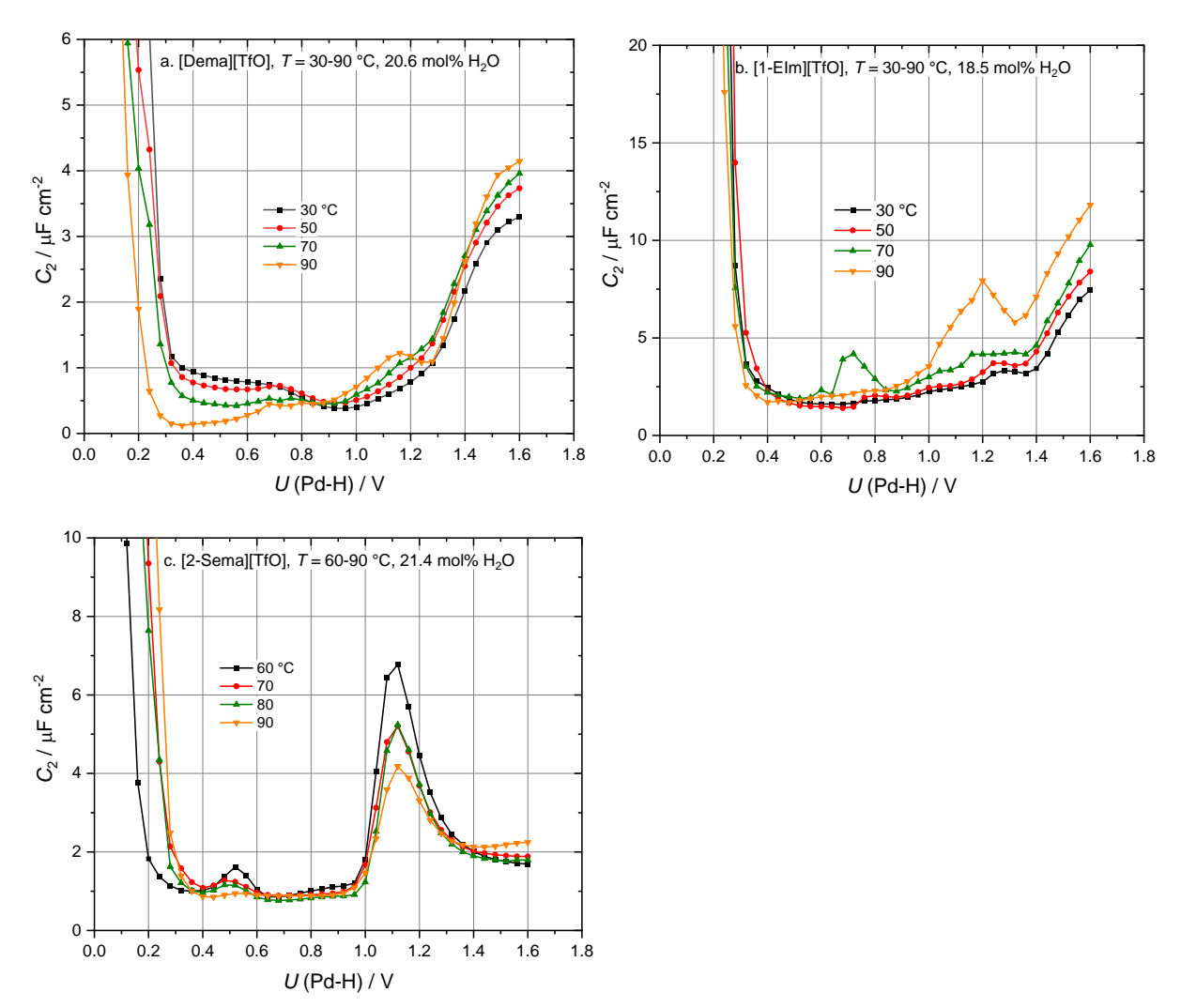


Table 1

	measuring conditions	[Dema][TfO]	[1-Elm][TfO]	[2-Sema][TfO]	suggested effects
pK _a value of cations / -	_	10.55	7.3	0.94	_
average vdW radius of cation / Å	_	4.75	4.48	4.90	ion structure
ratio vdW volumes cation: TfO / -	_	1.23	1.03	1.34	
$v = \text{ratio vdW volumes}$ $H_2O : \text{cation / -}$		0.180	0.196	0.173	
U _{PZC1} /V	T=30-90°C, x _{H20} ≈2-50mol%	0.36	0.44-0.48	0.28	metal-PIL(cation) interaction
T (α=0) / K	T=30-90°C, x _{H2O} ≈20mol%	192	211	262	interionic forces
average value of T_0^1 / K	T=30-90°C, x _{H2O} ≈2-50mol%	144	143	202	
α/-	T=90°C, x _{H2O} ≈20mol%	0.14	0.15	0.20	superposition/compensation of opposing effects for γ and (a-b), see below
γ/-	PZC, T=90°C, x _{H2O} ≈20mol%	0.37	0.23	0.15	compacity of ion layers / ion pairing
	U=0.8V ² , T=90°C, x _{H2O} ≈20mol%	0.35	0.18	0.10	
(a-b) / -	PZC, T=90°C, x _{H2O} ≈20mol%	33.2	49.8	54.8	- interionic forces
	U=0.8V, T=90°C, x _{H2O} ≈20mol%	35.4	62.7	83.6	
dα/d <i>T</i> / K ⁻¹	T=30-90°C, x _{H2O} ≈20mol%	8.1×10 ⁻⁴	9.8×10 ⁻⁴	2.0×10 ⁻³	superposition of temperature dependence of effects for γ and (a-b)
dγ ⁻¹ /d <i>T</i> / K ⁻¹	PZC, T=30-90°C, x _{H2O} ≈20mol%	-3.0×10 ⁻³	7.8×10 ⁻³	4.6×10 ⁻²	temperature dependence of compacity / ion pairing
d(a-b) ⁻¹ /d <i>T</i> / K ⁻¹	PZC, T=30-90°C, x _{H2O} ≈20mol%	2.1×10 ⁻⁴	1.2×10 ⁻⁴	1.1×10 ⁻⁴	temperature dependence of interionic forces

 $^{^{1}\}text{T}_{0}$ values derived from VFT plots of specific ion conductivity, $^{2}\text{typical cathode potential}$

Supplementary data:

0.2

0.0

0.6 0.8 1.0

U (Pd-H) / V

1.2 1.4 1.6

Fig. S1

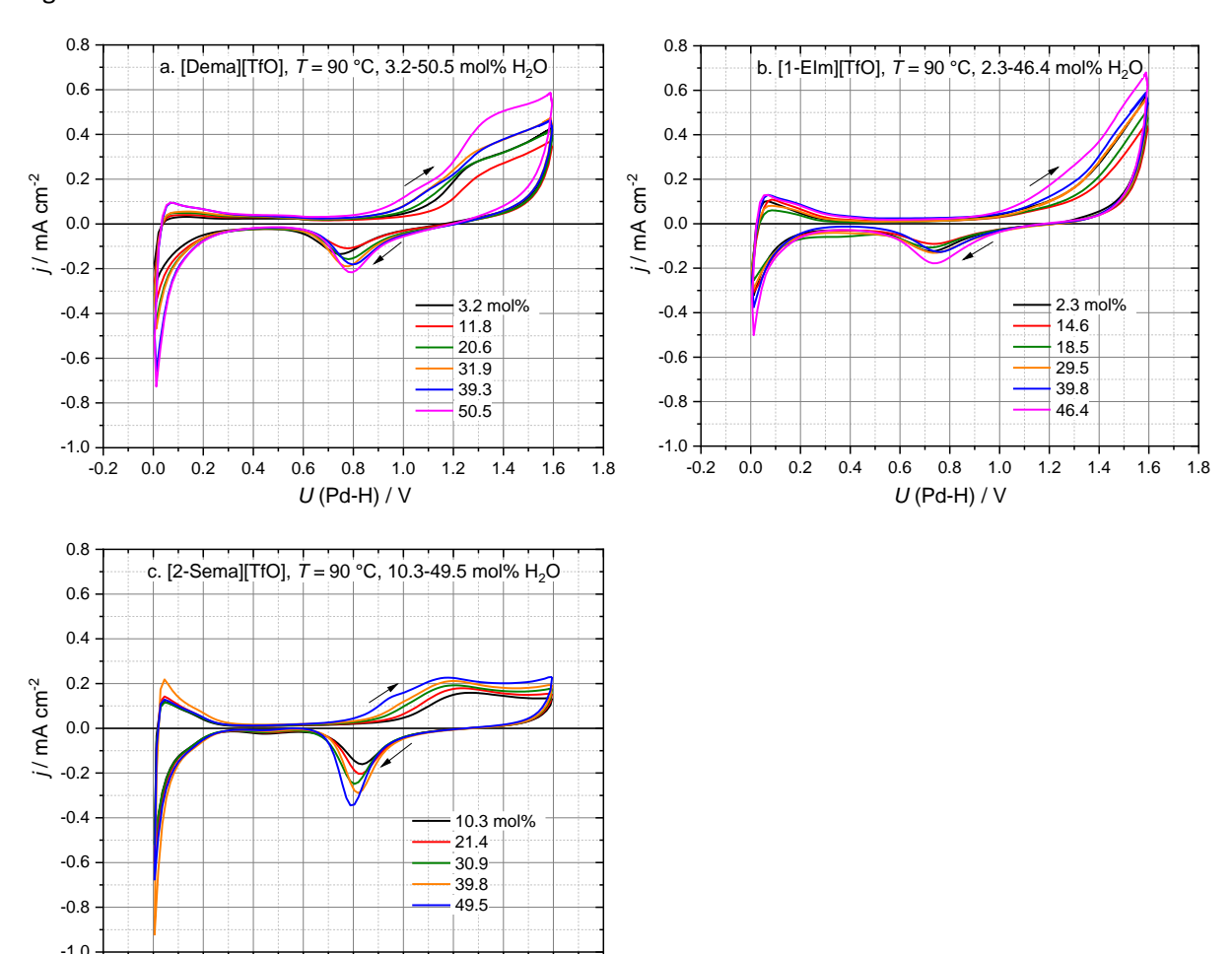


Fig. S2

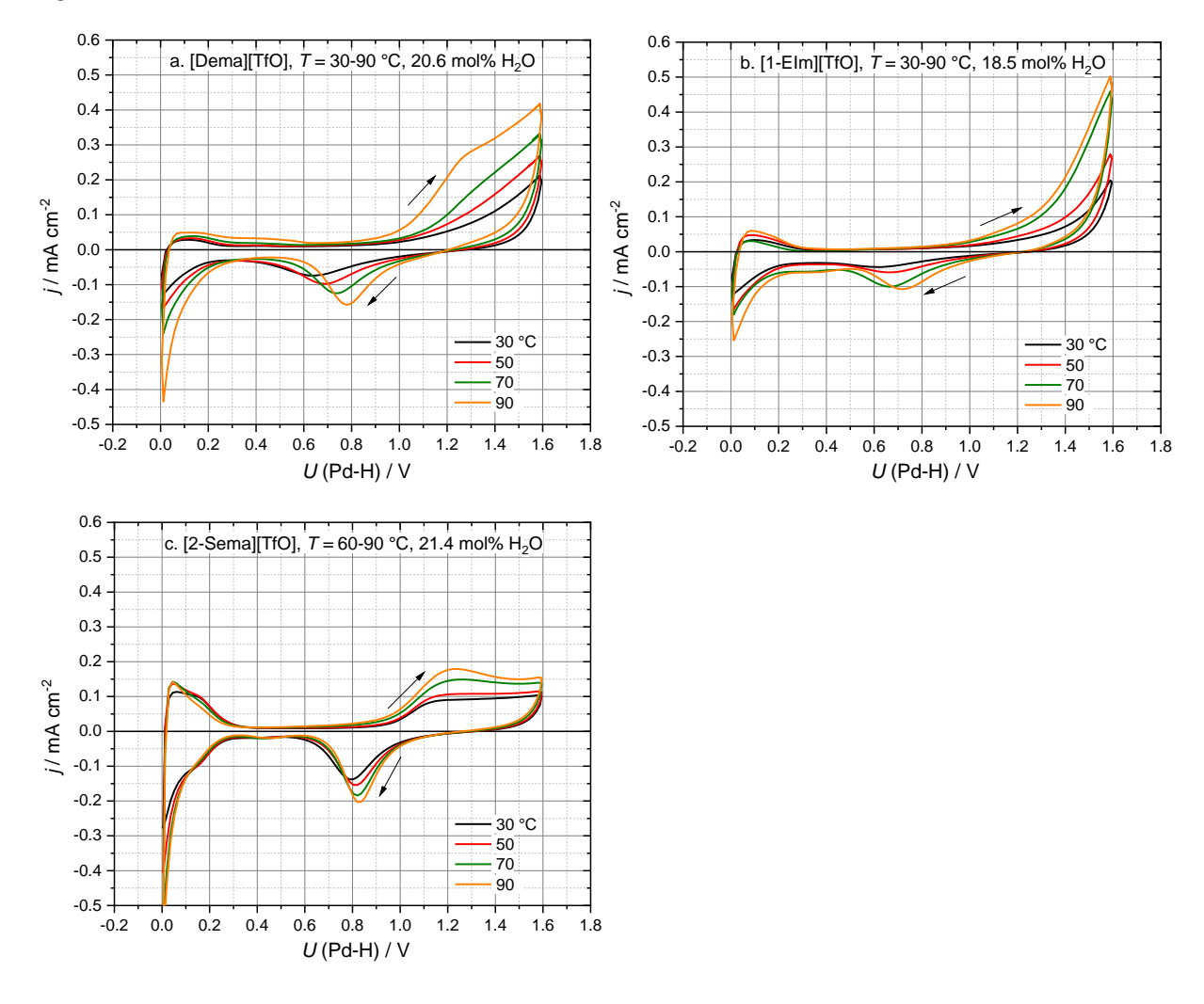


Fig. S3

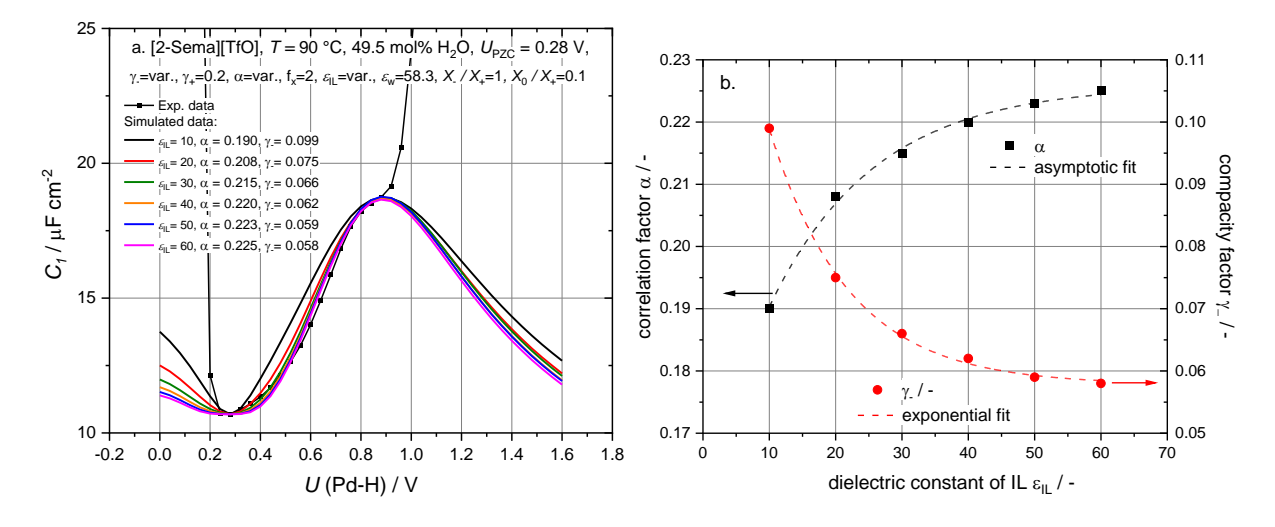


Fig. S4

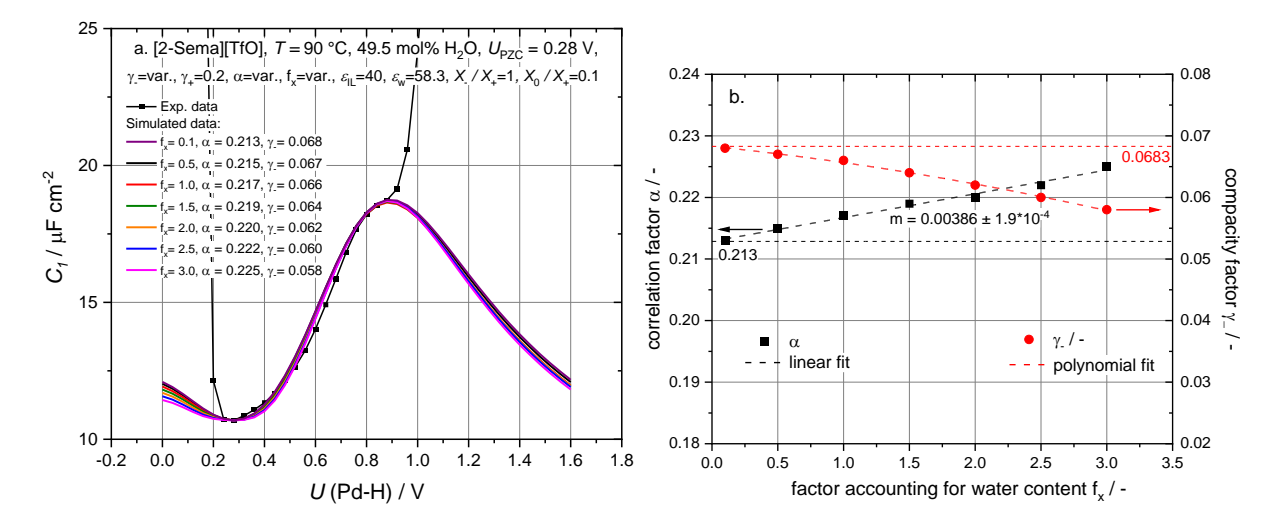


Fig. S5

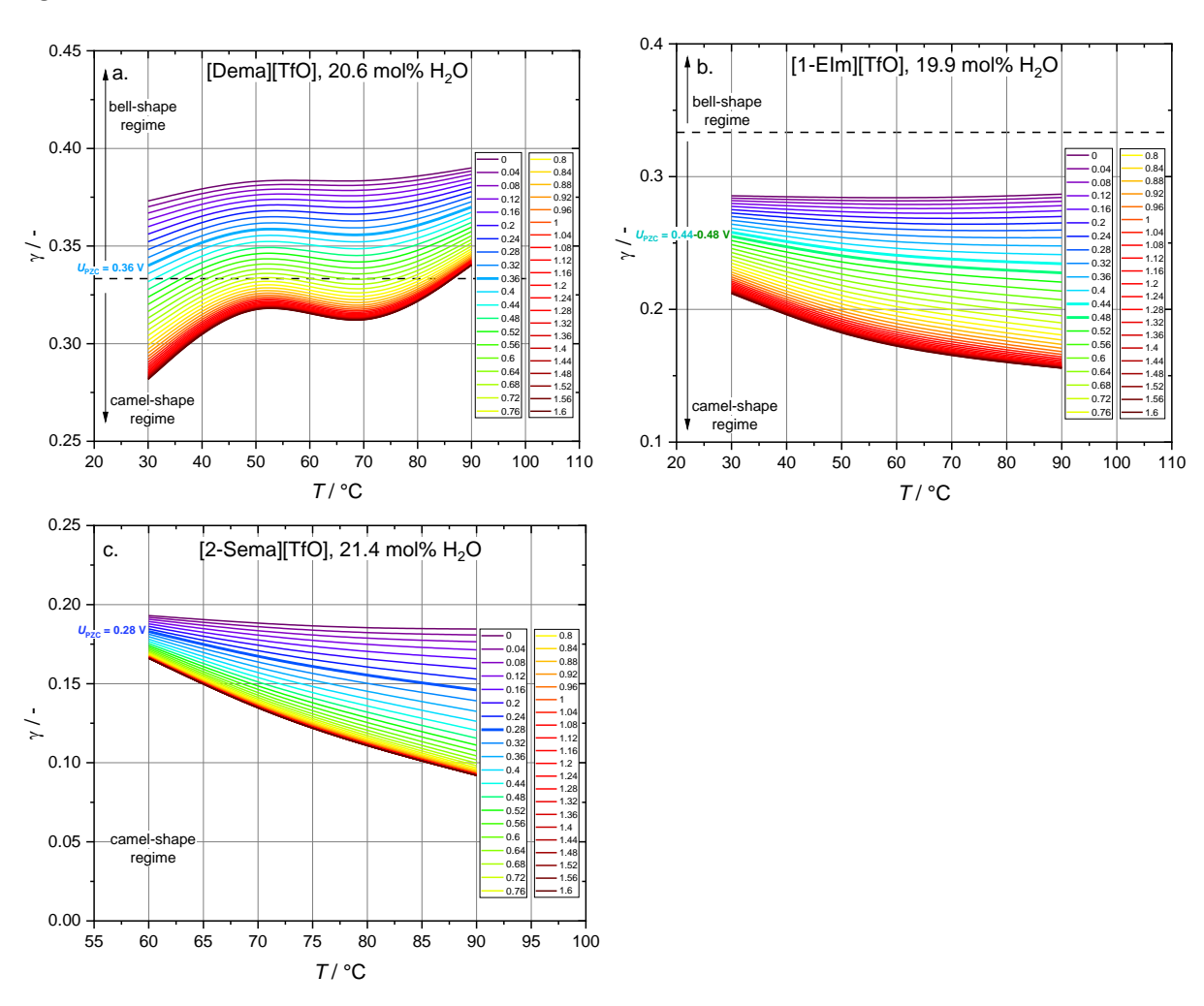


Fig. S6

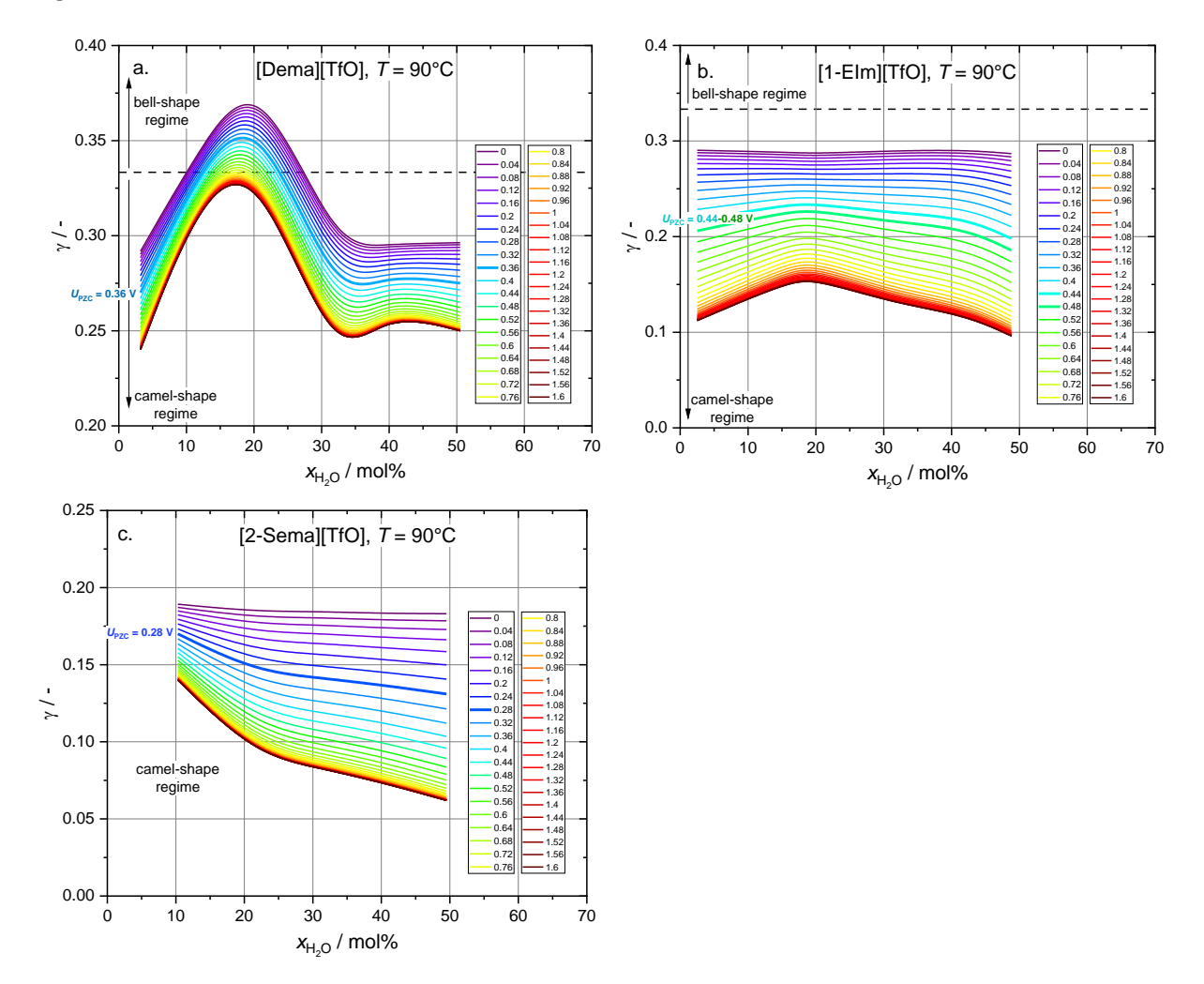


Fig. S7

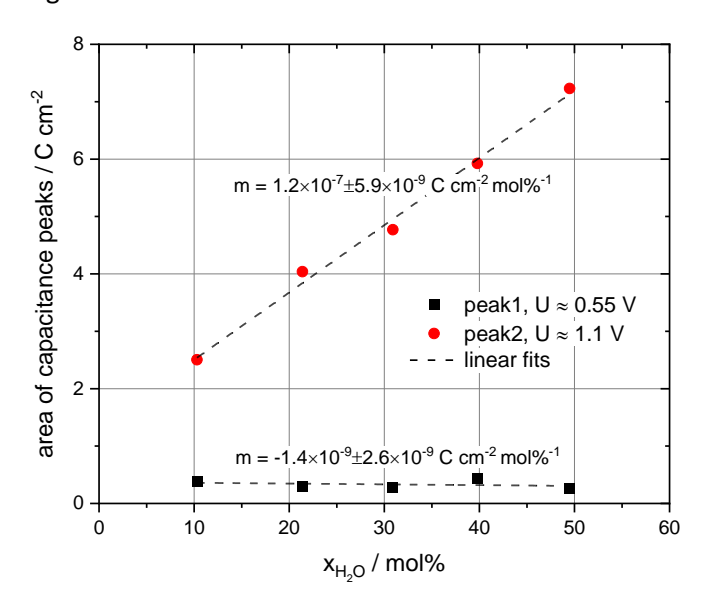


Fig. S8

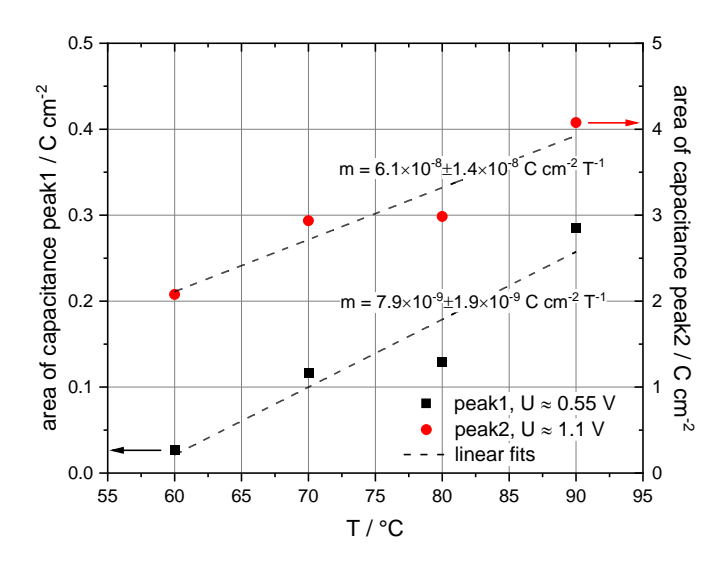


Fig. S9

